REFLECT DELIVERABLE D2.3

Mineral solubility and precipitation at high salinities

Summary:

Deliverable D2.3 reports the work performed in task 2.3 "Metal complexation and mineral precipitation" within the Reflect project. The task is divided into the subtasks 2.3.1 "Mineral solubility and precipitation kinetics", 2.3.2 "Mineral precipitation by impedance spectroscopy" and 2.3.3 "Modelling mineral solubility". A combination of experimental design, performed experiments and numerical modelling have increased the knowledge of mineral solubility and precipitation at high salinity condition in geothermal fluids.

Authors:

Morten Tjelta, Øyvind Brandvoll, Sissel Viig (IFE), Julianne Kummerow (GFZ), Arnault Lassin, Laurent André (BRGM)

This project has received funding from the European Union's Horizon 2020 research and innovation programme under grant agreement nº 850626.

Title:	Report on mineral solubility and precipitation at high salinities
Lead beneficiary:	IFE
Other beneficiaries:	GFZ, BRGM
Due date:	28.02.2023
Nature:	Public
Diffusion:	All Partners and public
Status:	Submitted Version 02
Document code:	REFLECT_D2.3
DOI:	https://doi.org/10.48440/gfz.4.8.2023.001
License information:	CC-BY-4.0
Recommended citation:	Tjelta, M., Brandvoll, Ø., Viig S.O., Kummerow, J., Lassin, A., André, L., The H2020 REFLECT project: *Deliverable D2.3 – Mineral solubility and precipitation at high salinities,* German Research Centre for Geosciences, DOI: https://doi.org/10.48440/gfz.4.8.2023.001
ORCID:	Julianne Kummerow: Scopus-ID: 36446009700 Sissel Viig: ORCID: 0000-0001-5871-4493 Morten Tjelta: ORCID: 0000-0002-3376-6702 Laurent André: ORCID: 0000-0002-8844-1585 Arnault Lassin: ORCID: 0000-0001-7414-7599
Related Data	10.5281/zenodo.7650170

Revision history	Author	Delivery date	Summary of changes and comments
Version 01	AL,LA	20.01.2023	Input subtask 2.3.3 (BRGM)
Version 02	SOV,MT, ØB/JK	25.01.2023/14.02.2023	Input subtask 2.3.1 (IFE)/Input subtask 2.3.2 (GFZ)

Approval status				
	Name	Function	Date	Signature
Deliverable responsible	Sissel Opsahl Viig	Task leader	16.02.2023	SOV
Reviewer	Katrin Kieling	Project manager	28.02.2023	KK
Project Coordinator	Simona Regenspurg	Project Coordinator	28.02.2023	SR

TABLE OF CONTENTS

1 EXECUTIVE SUMMARY

During geothermal fluid production changes in temperature and pressure may cause precipitation of solids and thereby influence the flow assurance in the system. Silica and calcite precipitation are some of the major technical issues experienced in geothermal power plants and for high saline systems the data available are limited. In this task the aim has been to increase the knowledge of mineral solubility and precipitation in such systems by combining experimental work (task 2.3.1 and 2.3.2) with numerical modelling (task 2.3.3).

In subtask 2.3.1 an experimental setup for investigating mineral solubility at high salinity conditions was designed and tested. The setup was further used to perform experiments to study silica solubility and kinetics in the temperature range 100 to 200°C and NaCl concentration range 50.92 to 338.09 g/kg H_2O. Both experiments to study dissolution kinetics and solubility at equilibrium conditions were performed. The main findings from the equilibrium solubility study are that silica solubility increases with temperature and decreases with salinity. Results from the kinetic experiments corresponds well with the results from the study performed at equilibrium conditions.

In subtask 2.3.2 a 4-point conductivity probe was designed for usage in batch reactors at temperatures up to 215 °C and a maximum system pressure of 70 bar. In particular, the probe was used both to indicate equilibrium conditions in calcite solubility experiments and to monitor the progressive depletion of the test solution in charge carriers (Ca^{2+}) during kinetic precipitation experiments by electrical conductometry. Calcite solubilities were determined at NaCl concentrations of 0 wt%, 5 wt%, 10 wt%, and 20 wt% in a temperature range of 24 to 213 °C and CO_2 pressures of 10 to 50 bar. It was found that the calcite solubility decreases exponentially with temperature and increases with CO_2 pressure. The solubility is lowest in pure water, increases to a maximum between 5 and 10 wt% and decreases gradually at higher salinities.

In subtask 2.3.3 a model for silica precipitation was developed that accounts for several mechanisms described in the literature. These mechanisms include nucleation, aggregation, aging and growth. Their respective role varies with pH, initial dissolved silica content ($m_{SiO_2}^{init}$) and ionic strength (I). The model describes the formation of both nanocolloidal and microscopic amorphous silica, and the evolution of their relative amounts with time.
The model was calibrated on literature data that were obtained from experiments made on synthetic solutions. Then, it was tested on literature data that were measured on geothermal waters. The range of conditions of application are the following: $3 < pH < 8$, $0 < m_{SiO_2}^{init} < 20.8$ mmol·kg^{-1}, $0 < I < 0.5$ mol·kg^{-1}, at 25 °C.
In addition to precipitation, modelling work was carried out to simulate the quartz dissolution experiments done in subtask 2.3.1. Modelling used a kinetic rate law based on the transition state theory. Results suggest that, despite the sand used for the experiments was made of quartz, the measured SiO_2 concentrations rather correspond to amorphous silica, for both the kinetic behaviour and the final equilibrium state.

2 TASK 2.3.1 - MINERAL SOLUBILITY AND PRECIPITATION KINETICCS

2.1 INTRODUCTION

During geothermal fluid production changes in temperature and pressure may cause precipitation of solids and thereby influence the flow assurance in the system. In this task the solubility and precipitation of silica have been studied as a function of salinity and temperature. Temperature range have been from 100 to 200°C and NaCl concentration range studied was from 50.92 to 338.09 g/kg H_2O. An important part of the work has been design and development of experimental setup for these harsh conditions.

Experiments have been carried out at a constant pressure around 40 bar, which is believed to be representative in the temperature range studied in this task (100-200 °C). According to density models for the pure H_2O [IAPWS] and H_2O-NaCl [OLI] the liquid density is fairly insensitive to pressure variations in this temperature region, and water is often treated as incompressible. Figure 1 shows the density of pure water and 300 g/L NaCl as a function of temperature and pressure. Since silica solubility can be expressed as a function of temperature and density [e.g. A&D model] it will in practice be a function of temperature only in the region where density changes are negligible. Although the abovementioned considerations apply for thermodynamic solubility, there is no indication of pressure affecting the kinetics in the incompressible region.

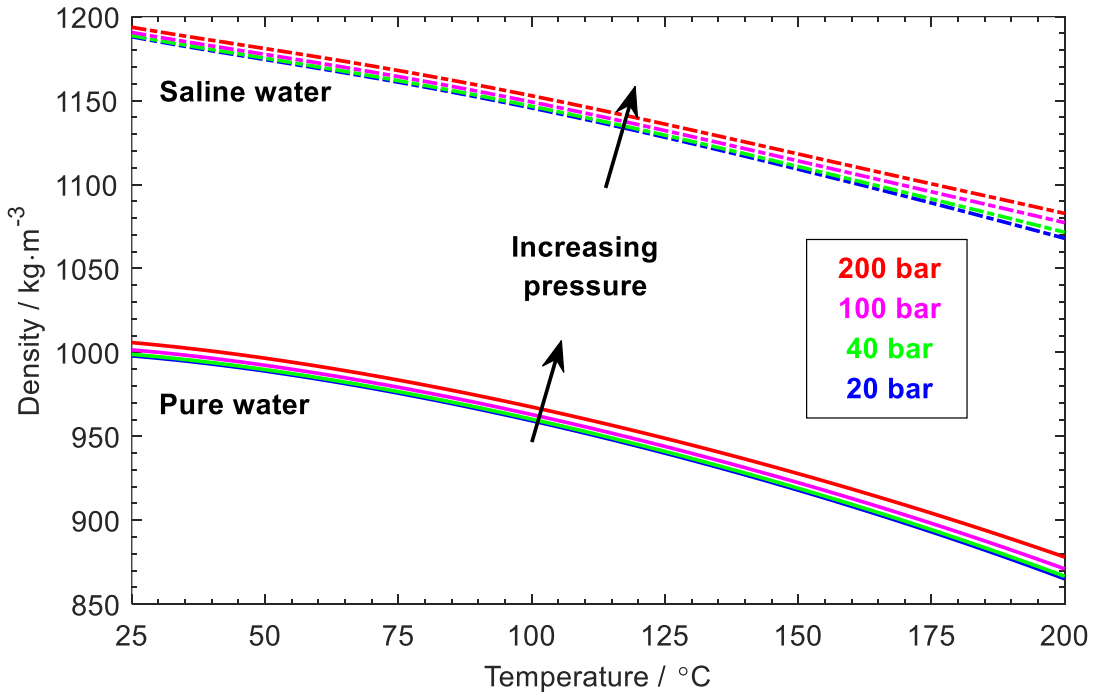

Figure 1: Density as a function of temperature and pressure for pure water and 300 g/L NaCl as calculated using OLI

Pressure may have implications for phase behaviour in a binary electrolyte where phase envelopes are encountered. At pressures above the two-phase pressure of the pure solvent this should not be an issue. This can be seen in Figure 2, where solubility limits for the H_2O-NaCl binary are plotted using values obtained from Driesner and Heinrich (2007).

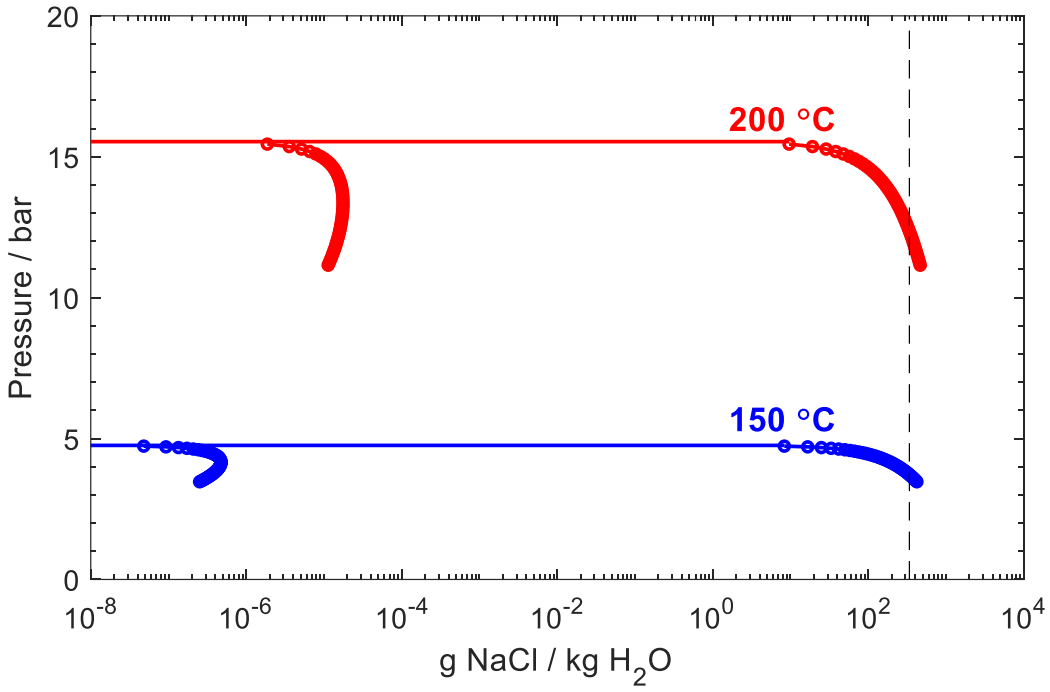

Figure 2: H2O-NaCl binary system for the 150 and 200 °C isotherms according to Driesner and Heinrich (2007). The grey dashed line marks 300 g/L (338 g/kg) used in this work

2.1.1 Relating dissolution to precipitation

The ideal experiment would be direct measurement of precipitation kinetics. This should be done whenever possible. At lower temperatures, say up to 200 °C, kinetics is fairly slow and it is possible to follow precipitation by analyzing samples. This approach was followed by Dixit et al. (2016) when they analysed fluid samples taken as a function of time and measured monomeric silica concentration using the molybdenum blue method. A real fluid of around 250 °C with around 600 mg/L SiO_2 was used as a source, but the kinetic measurements were carried out after cooling to a temperature in the range 25-90 °C.

At higher temperatures precipitation is expected to occur almost instantaneously when the solution is supersaturated, meaning that any sample taken in practice will be that of the saturated solution. In order to capture precipitation kinetics some in-situ information, such as a window or a probe, is required. Some labs have developed HPHT reactors with sapphire windows (double or even triple) which could in principle be coupled with an in-situ method such as Raman spectroscopy.

To overcome experimental challenges with direct precipitation experiments, dissolution experiments have been carried out instead. The theory arguing how results can be applied to obtain precipitation information is described in the papers by Rimstidt and Barnes (1980) and Tester et al. (1994). Rimstidt and Barnes (1980) measured silica dissolution up to 300 °C in pure water. Kinetic information was obtained by taking fluid samples at intervals to determine the H_4SiO_4 concentration. Based on absolute rate theory, where reactions pass through an activated complex with an energy maximum, a relation between the forward and backward (i.e. dissolution and precipitation) reactions was put forward. The authors noted that their work is valid for silica and relatively pure water, and that the rate constants may be complex

functions of pH and salinity. The aim of the present work is to follow this approach and provide rate constants for systems with higher salinity.

Silica dissolution rate can, in its simplest form, be described as a function of the solid surface area, the fluid volume and a forward rate constant (see e.g. van Lier et al. (1960) or Cournoyer et al. (1975).

$$\left(\frac{dC_{SiO2}}{dt}\right)_f = k_f \frac{A_{surf}}{V_{fluid}} \tag{1}$$

In an equilibrium situation, the forward (dissolution) and backward (precipitation) rates are equal, meaning that

$$K_{eq} = \frac{k_f}{k_b} \tag{2}$$

Such a relation is valid in the case of no nucleation only, i.e. when the rate of growth and dissolution of the same particle surface are equal. Silica dissolves as silicic acid according to

$$\mathrm{SiO_2} + 2\mathrm{H_2O} = \mathrm{H_4SiO_4} \quad , \quad K_{eq} = \frac{a_{\mathrm{H_4SiO_4}}}{a_{\mathrm{SiO_2}} a_{\mathrm{H_2O}}^2} \tag{3}$$

For the case of pure silica the solid silica activity is one. In (relatively) pure water the water activity can be further taken as one and $K_{eq} = a^{eq}_{\mathrm{H_4SiO_4}}$. This allows the backward rate constant to be expressed as a function of the forward one and the equilibrium dissolved silica concentration (note the negative sign since precipitation decreases dissolved silica while rate constants are kept positive)

$$\left(\frac{dC_{SiO2}}{dt}\right)_b = -k_b a_{\mathrm{H_4SiO_4}} \frac{A_{surf}}{V_{fluid}} = -\frac{k_f}{K_{eq}} a_{\mathrm{H_4SiO_4}} \frac{A_{surf}}{V_{fluid}} \tag{4}$$

Furthermore, the net rate of change can (with unit activities for water and solid silica) be expressed as

$$\left(\frac{dC_{SiO2}}{dt}\right)_{net} = \left(\frac{dC_{SiO2}}{dt}\right)_f + \left(\frac{dC_{SiO2}}{dt}\right)_b = k_f \frac{A_{surf}}{V_{fluid}} \left(1 - \frac{a_{\mathrm{H_4SiO_4}}}{a^{eq}_{\mathrm{H_4SiO_4}}}\right) \tag{5}$$

For systems with low levels of dissolved silica the net change equation reduces to the forward equation while for large supersaturation the limit goes to the backward equation. It is customary to further simplify rate equations by replacing activity with concentration. For dilute solutions with low ionic strength this is justified, while for non-ideal solutions this simplification should strictly only be applied to the full net rate equation where activity coefficients (cf. $a = \gamma c$) cancel.

The above equations have been formulated using molar concentration and fluid volume. They may easily be recast using molal and fluid mass. Either way, the unit of the rate constant is $mol \cdot m^{-2} s^{-1}$.

2.2 EXPERIMENTAL

2.2.1 Materials

The silica material used as solid substrate for the dissolution studies was pro analysis sea sand (purified by acid washing and calcinated for analysis) from Merck. The sand grain size (125-250 µm) included in the experiments was obtained by sieving the material. The sieved powder was washed with tap water to remove fine grains from the samples, and dried prior to experiments. Sodium chloride (NaCl) was purchased from Merck.

2.2.2 Experimental setups and methods

2.2.2.1 Setups for testing silica solubility and kinetics

For experimental testing of silica solubility and dissolution kinetics at high saline conditions two types of experimental setups were evaluated: stirred autoclaves and packed static columns. The two approaches are described more in details in 2.2.2.1.1 and 2.2.2.1.2.

2.2.2.1.1 Stirred autoclave

Two different 100 ml autoclaves were available and considered for use in the project. Figure 3 shows pictures of the two options: "Limbo 350" (Buchi GlasUster) high P/T reactor and a "Vivor" pressure vessel from Premex. Materials of construction are titanium (Ti316) and Hastelloy 276, respectively. The Limbo is a complete multi-port vessel with proportional–integral–derivative (PID) temperature controller, whereas the Premex vessel is considerably simpler in design and operation, having only one assembly bolt, one sampling/charge port, heating jacket + PID. Agitation in the latter is achieved by polytetrafluoroethylene (PTFE) stirrer bar and stirrer plate.

Stirred autoclaves have some notable advantages in heterogenous reactions, particularly that agitation of the solid/liquid reactants ensures that mass-transfer (surface reactant/product diffusion) is not overall rate-determining. One also has absolute control of the reactants as the reactor would be rinsed and charged with new materials for each experiment. There are several drawbacks, however; the Limbo 350 becomes impractical due to multiple assembly bolts and expensive replacement wetted parts (seal). The study of multiple combinations of salinities and temperatures would require many reactor seals and there would be considerable turn-around between experiments. Furthermore, the material of construction (Ti316) is not recommended for high temperatures and high chloride concentrations. Additionally, such a vessel can only run a singular condition at a time. Based on these considerations the autoclaves were not included in further work in the project.

Figure 3. Left: Buchi "Limbo 350" and Right: Premex "Vivor".

2.2.2.1.2 Packed static columns

The second type of setup consists of packed static columns. Such setup gives the possibility to perform several experiments in parallel, e.g. experiments with different brine concentrations or composition. A sketch of the setup is given in Figure 4 and pictures are given in Figure 5. Maximum four columns (length 40 cm, i.d. 10.22 mm, stainless steel SS316) packed with the material to study can be placed in parallel within the setup. Porous metal frits (HC276) are placed at the outlet and inlet of the columns to prevent entrainment of the material. Approximately 50 g of dried SiO_2 powder is required to fill a column completely and the pore volume was measured gravimetrically to be approximately 15 ml. Two Gilson 307 high performance liquid chromatography (HPLC) pumps are included in the setup. One for filling and displacing column pore fluid and one for diluting the fluid prior to sampling, preventing precipitation of dissolved silica due to depressurization and cooling. Pressure was maintained by a dome loaded backpressure regulator (BPR) from CoreLab at the column outlet and liquid samples were collected using a fraction collector (Gilson FC203B). The setup of columns and inlet/outlet valves was placed in a heating cabinet (Memmert). Initial tests showed that the opening of the heating cabinet to operate inlet and outlet valves, introduced thermal - and hence pressure instabilities, i.e. oscillating pressures. To reduce this effe ct, the columns were thermally insulated in subsequent experimental campaigns.

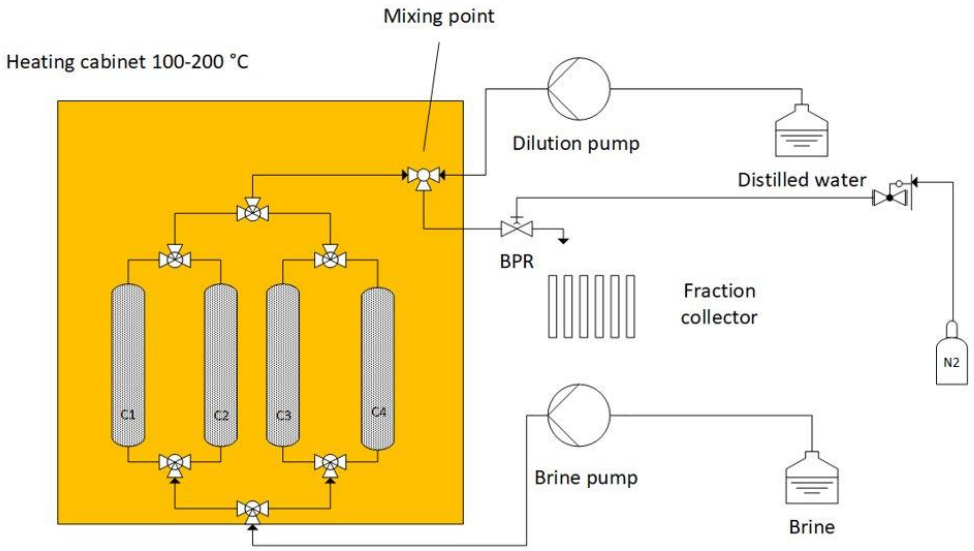

Figure 4. Sketch of setup for testing silica solubility at temperature and pressure.

Figure 5. Pictures of the setup with packed columns.

2.2.2.2 Test procedure and validation

The experimental setup described in 2.2.2.1.2 was selected for further testing and method development. The columns are flooded with the defined fluid at a low flow rate and pressurized initially to 25 bars while temperature is increased slowly to the desired level. For initial testing temperature was set to 175°C. The time of start is noted, the brine pump is shut off, and the individual columns isolated by closing inlet and outlet valves. After a period (hours, days, or weeks) samples are withdrawn from the columns and diluted at the mixing point by re-opening the valves and operating both HPLC pumps. A dilution factor of 8.5 is selected to prevent precipitation. For each sampling five samples of 2 ml is collected (totally 10 ml of fluid). The two first samples are considered to contain mainly dead volumes from tubing, fittings and valves and are therefore discharged. The three last samples represent the pore fluid from the column. These samples are analysed for Si and NaCl concentration. The NaCl concentration was analysed to keep control of the dilution step of the sampling process.

Two series of column exposures were carried out in the verification step: 1) static tests using distilled water at 175°C with the aim of overall verifying the concept and sampling method, analytical protocol etc. 2) Long term exposure to 200 °C, 100 g/L NaCl solution to look for possible corrosion effects on stainless steel components in the setup. During these tests it was found that the proposed sampling method was feasible and repeatable. Furthermore, significant corrosion was observed during these tests, in the form of orange coloration and pink/reddish precipitates. These effects were mitigated by degassing (helium sparging) of brine and dilution water. The valves exposed to heat were severely impacted by the temperature of 200°C and were typically replaced after 1-2 months run time.

In the method development phase two different grain intervals (63 – 125 µm and 125 – 250 µm) of the sand from Merck were tested. The results are given in Figure 6. Similar Si concentrations were detected for the two grain intervals and in the further experiments the grain interval 125-250 µm was selected.

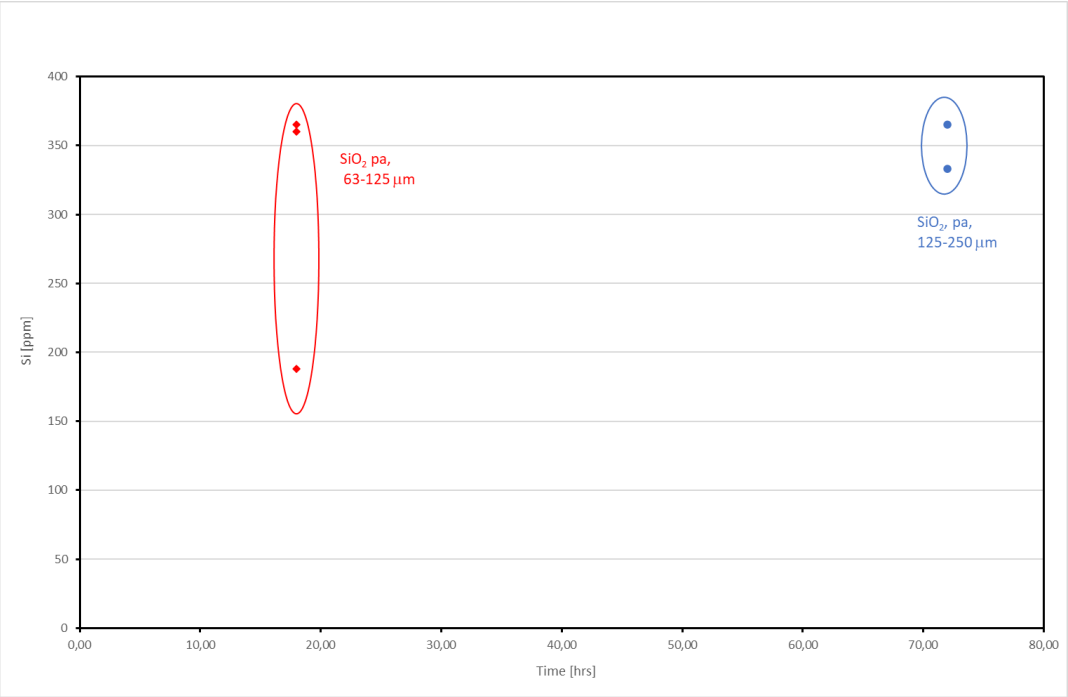

Figure 6. Dissolved silica vs. time for initial solubility tests. Two different quartz samples were used, as indicated by the ovals and corresponding text. Test performed at 175°C with distilled water.

2.2.2.3 Experimental parameters

Using the packed column setup described in chapter 2.2.2.1.2, two different types of experiments were performed. First, experiments were conducted to study equilibrium conditions for silica at five different temperatures (100, 125, 150, 175 and 200°C) and four salinities (NaCl concentrations 50.92, 103.64, 215.65 and 338.09 g/kg H_2O). The columns containing SiO_2 and NaCl solutions where isolated for a reaction time of six days, a proper time for ensuring equilibrium conditions in the columns. The second type of experiment was kinetic experiments to study solubility and dissolution kinetics. In these experiments the columns were isolated for different time periods (from 1 hour up to 144 hours) to study solubility as a function of time. These tests were conducted at 200°C with NaCl concentration 50.92 g/kg and 338.09 g/kg H_2O.

2.2.2.4 Quantification of SiO_2 and NaCl concentrations

SiO_2 and NaCl concentrations were analysed using inductively coupled plasma mass spectrometry (ICP-MS) or inductively coupled plasma optical emission spectrometry (ICP-OES). The elements Si and Cl (ICP-MS) or Si and Na (ICP-EOS) were detected.

2.3 RESULTS AND DISCUSSION

As described in 2.2.2.3, two types of experiments were performed during the project period. First, SiO_2 solubility experiments at equilibrium concentrations were carried out (experimental details given in 2.2.2, results given in 2.3.1). Then, kinetic experiments with SiO_2 were performed at 200°C with NaCl concentration 50.9 g/kg H_2O and 338.09 g/kg H_2O (experimental details given in 2.2.2, results given in 2.3.2).

2.3.1 SiO_2 solubility at equilibrium

The results from the solubility experiments at equilibrium are given in Figure 7 and Figure 8. In the first figure the SiO_2 concentrations are plotted as a function of temperature for the different NaCl concentrations included while in the second figure the SiO_2 concentrations are plotted as a function of NaCl concentration for the different temperatures. All SiO_2 concentrations are plotted as mol SiO_2 per kg H_2O. The main findings from these experiments can be summarized as follows:

- The solubility of SiO_2 increases when the temperature increases.
- The solubility of SiO_2 decreases when the NaCl concentration increases.

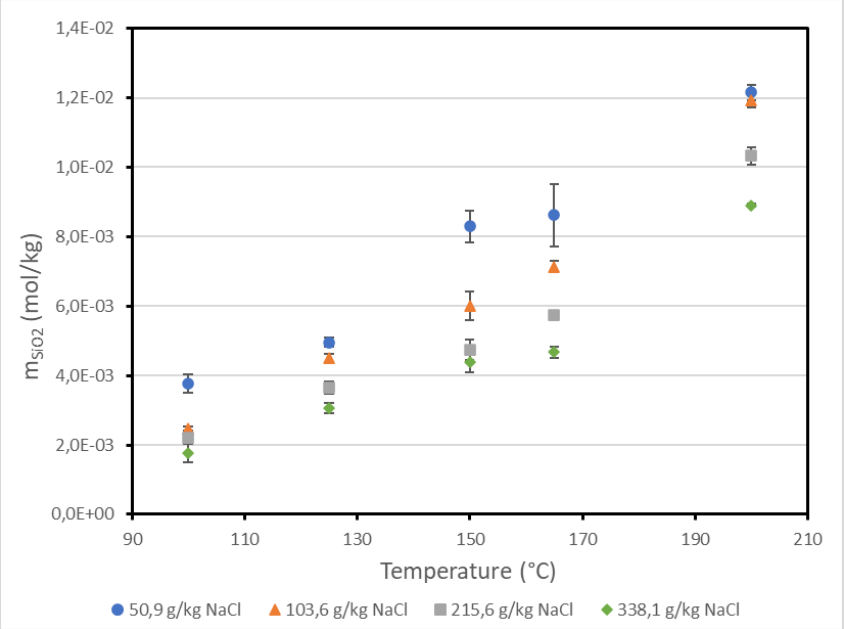

Figure 7. Results from SiO_2 experiments at equilibrium plotted as function of temperature. The SiO_2 concentration is presented as mol per kg H_2O.

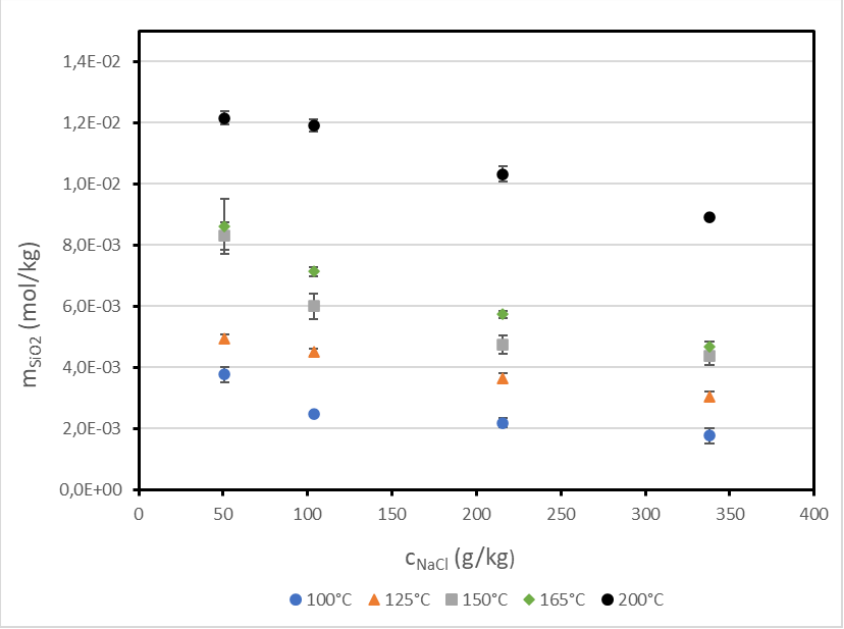

Figure 8. Results from SiO_2 experiments at equilibrium plotted as function of NaCl concentration. The SiO_2 concentration is presented as mol per kg H_2O.

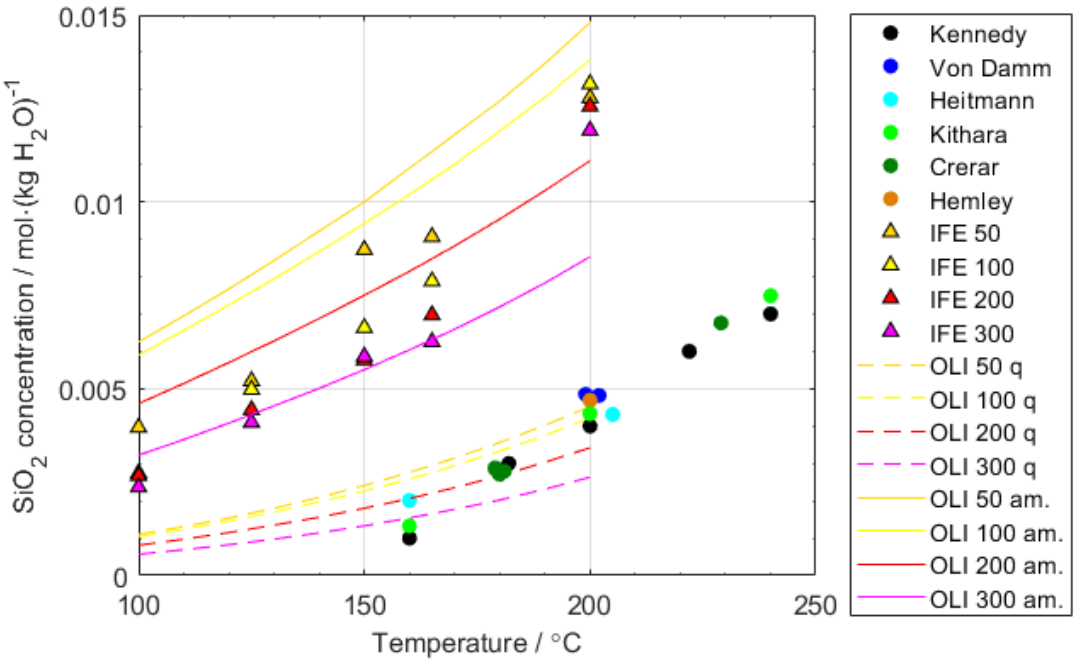

Figure 9: Silica solubility as a function of temperature. Circles are literature values for quartz, triangles are data from this study with NaCl in g/L as indicated in the legend and lines are values calculated using the OLI software for both quartz (q) and amorphous silica (am.).

Figure 9 shows equilibrium silica solubility values obtained in this study (triangles) compared with literature values (circles) and values obtained using commercial software (lines). Literature values were obtained along the vapor-liquid equilibrium (VLE) curve, except Heitmann (1964) used a higher pressure. All literature sets are for pure water, except Von Damm (1991) who did the study in 0.5 M NaCl. Calculations were done for 40 bar to coincide with the experiments carried out in this work and the figure includes values for quartz (dashed lines) and amorphous silica (solid lines).

Values obtained in this work are close to calculated values for amorphous silica, which is surprising considering that characterization (XRD) found mainly quartz in the studied material (chapter 2.3.3). The XRD results indicate that the starting material is crystalline and consisting mainly of quartz, albeit with some minor (unidentified) impurities which is commonly the case for natural samples. EDS (energy dispersive spectroscopy) (chapter 2.3.4) showed that the major impurity was aluminum and alkali (Na, K), suggesting some (Na,K)Al-silicate. Both calculation and experiments suggest decreasing solubility with increasing NaCl concentration, i.e. a salting out effect. This contrasts Dove and Rimstidt (1994) who stated that quartz solubility is larger in saline solutions than in pure water (cf. salting-in effect). This was explained to be a consequence of Na+ and/or Cl- ions affect the hydrogen bonding properties of water. In a kinetic study by Rimstidt and Barnes, (1980), however, it was stated that salt reduces the water activity and hence silica solubility.

2.3.2 KINETICS

The results from kinetic experiments to study SiO_2 solubility and dissolution kinetics at 200°C are presented in Figure 10 and Figure 11 for NaCl concentration 50.9 g/kg and 338.09 g/kg H_2O respectively. The main findings from these experiments are:

- For NaCl concentration 50.9 g/kg and temperature 200°C the SiO_2 concentration stabilizes at approximately 1.2 e^{-2} mol/kg H_2O.
- For NaCl concentration 338.09 g/kg and temperature 200°C the SiO_2 concentration follows two trends, one the stabilizes around 9.0e^{-3} mol/kg H_2O and one the stabilizes around 5.0e^{-3} mol/kg H_2O.

Several experiments at the same conditions were performed to study solubility kinetics. The results from all experiments have been included in the figures presented below. The experiments have been named based on the period they were conducted (e.g January 2021, April 2021 etc) and labelled with different colors in the presented figures.

In general, the equilibrium concentrations achieved in these experiments corresponds well with the measured equilibrium concentrations presented in 2.3.1, except for the results obtained in May_June 2022 presented in Figure 11. For the experiments at 200°C and NaCl concentration 338.09 g/kg H_2O (Figure 11) two different trends are observed, one that stabilizes around 9.0e^{-3} mol/kg H_2O and one the stabilizes around 5.0e^{-3} mol/kg H_2O. During the experiment conducted in May and June 2022 a leakage appeared at the inlet tube placed before the experimental column. As a result, the experiment was paused to make corrections to the setup before the experiment continued. After restart of experiment (May_June 2022 Remaining part of experiment) a different trend in solubility kinetics were observed (black dots in Figure 11).

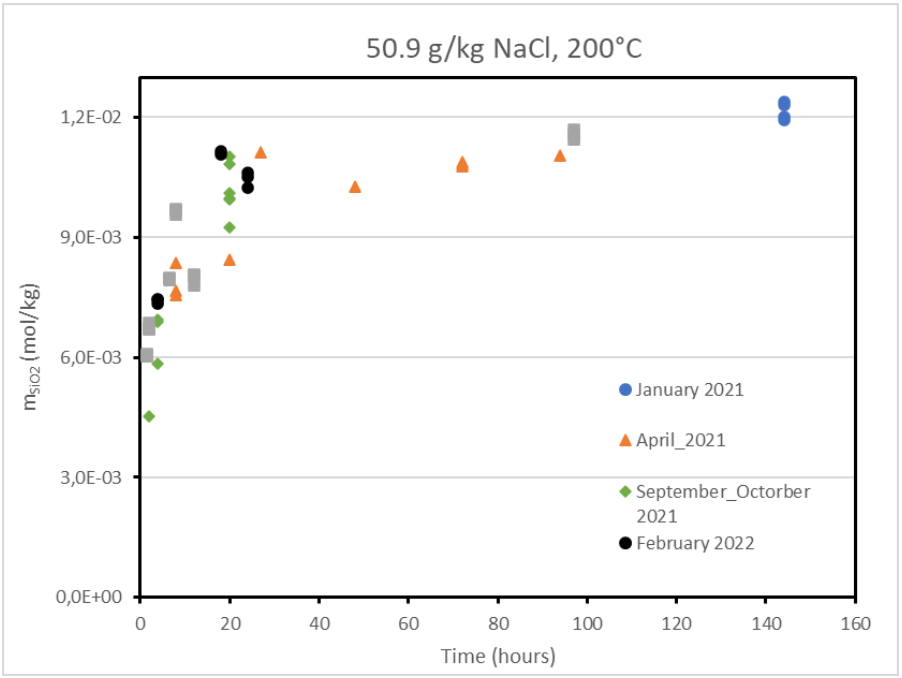

Figure 10. Results from kinetic dissolution experiments at 200C with 50.9 g/kg NaCl H_2O.

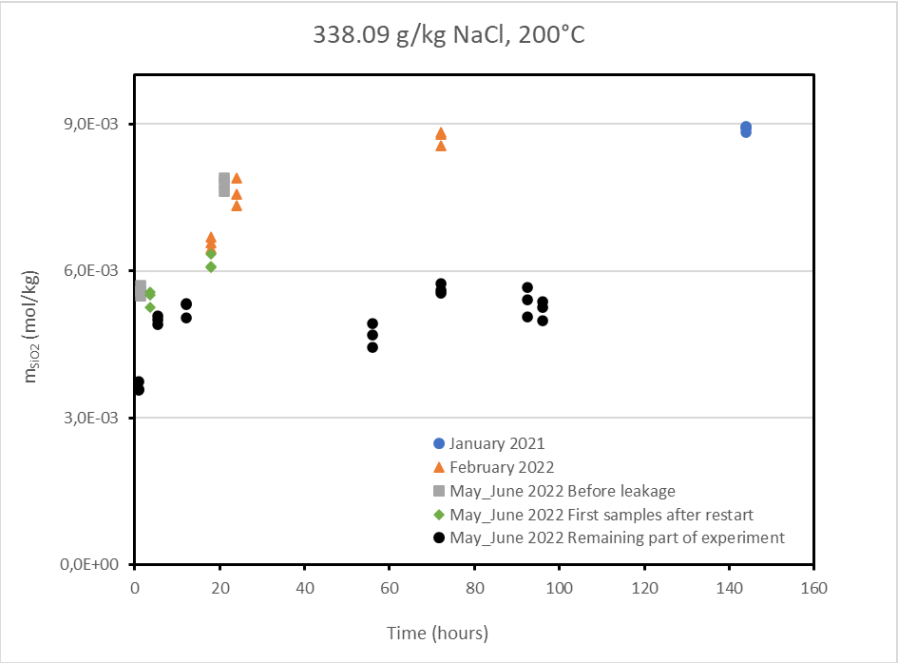

Figure 11. Results from kinetic dissolution experiments at 200C with 338.09 g/kg NaCl H_2O.

2.3.3 Characterization of SiO_2

Prior to start-up of experiments the sand included in experiments was characterized by different methods: BET for surface area measurement, PSD for particle size distribution and X-ray diffraction analysis (XRD) for determination of crystallographic structure. The BET and PSD data are given in Table 1, while the XRD data is given in Figure 12 and Figure 13. The XRD data shows that the sample mainly consist of low-quartz (minimum 95 % w/w) with a few unidentified impurities. When searching for impurities components containing Si, Mg, Ca, Fe, Al, O, H have been in focus.

After exposure the powders still consists of mainly quartz, as seen in Figure 14, where diffractograms of unexposed and exposed powders are compared. The main difference is that exposed powders contain some NaCl (halite) that most likely precipitated during the shut-down procedure (described in 2.3.2).

Table 1: Measured BET and PSD data for the silica material used for the dissolution studies.

	Pro analysis sea sand (Merck)
BET surface area	0.6921 m^2/g
PSD surface weighted mean	117.717 µm
PSD volume weighted mean	127.099 µm

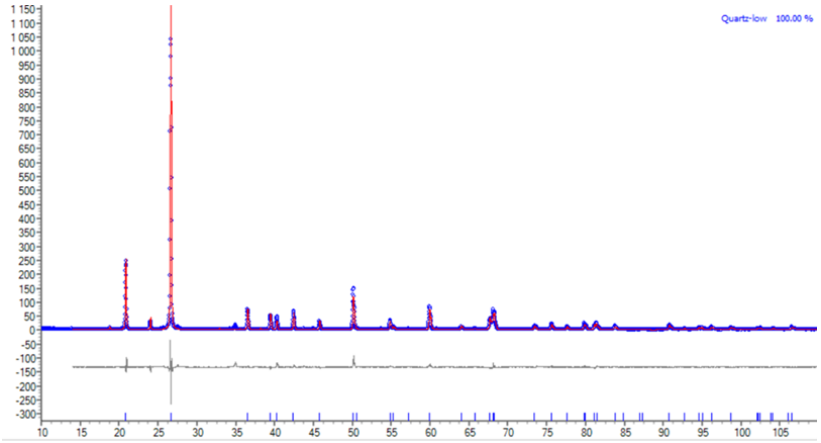

Figure 12. XRD data (linear plot) for the sea sand included in experiments. Blue curve is the measured data, red curve is the calculated data for "low-quartz" and the grey curve is the difference between the blue and red curve.

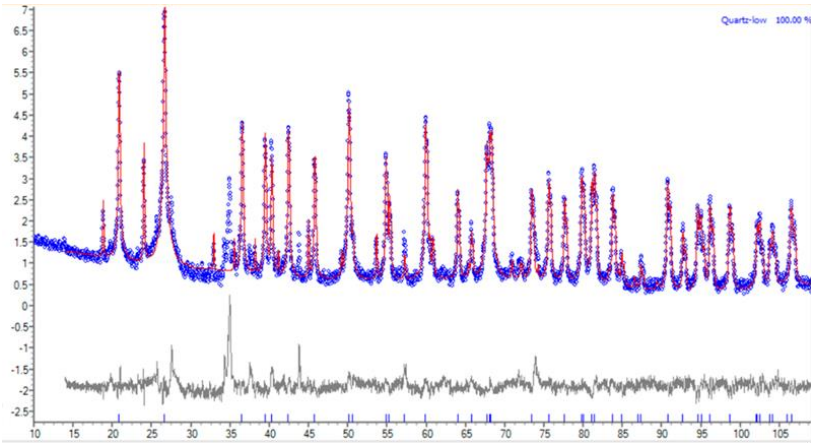

Figure 13. XRD data (logarithmic plot) for the sea sand included in experiments. Blue curve is the measured data, red curve is the calculated data for "low-quartz" and the grey curve is the difference between the blue and red curve.

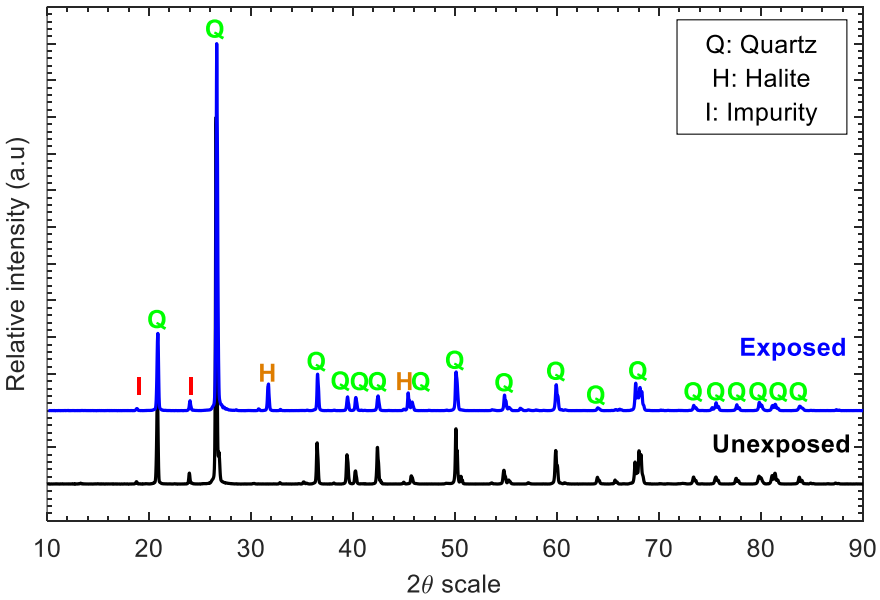

Figure 14: XRD data of unexposed (black) and exposed (blue) silica powders

2.3.4 SEM results

SEM (scanning electron microscopy) images of unexposed and exposed silica can be seen to the left and right of Figure 15, respectively. Direct comparison of small regions should be exercised with caution, but it appears that a slight roughening of the surface takes place during exposure. The macroscopic particle size, however, remains essentially unchanged before and after exposure (cf. Figure 16).

Figure 16 shows EDS maps of unexposed (left) and exposed (right) silica powders used in these experiments. Quantified data are included in Table 2 and Table 3, where lines have been colour-coded to help locate regions in the map. Most regions (orange) are essentially pure silica with minor Al impurity. Some grains or regions (magenta, purple) are enriched in Al and K, suggesting some aluminium silicate. Unexposed powders also contain some minor spots rich in Ti (green) or Fe and Cr (blue). Such regions can also be found in the exposed specimen, and here regions with precipitated NaCl are also present in agreement with XRD results.

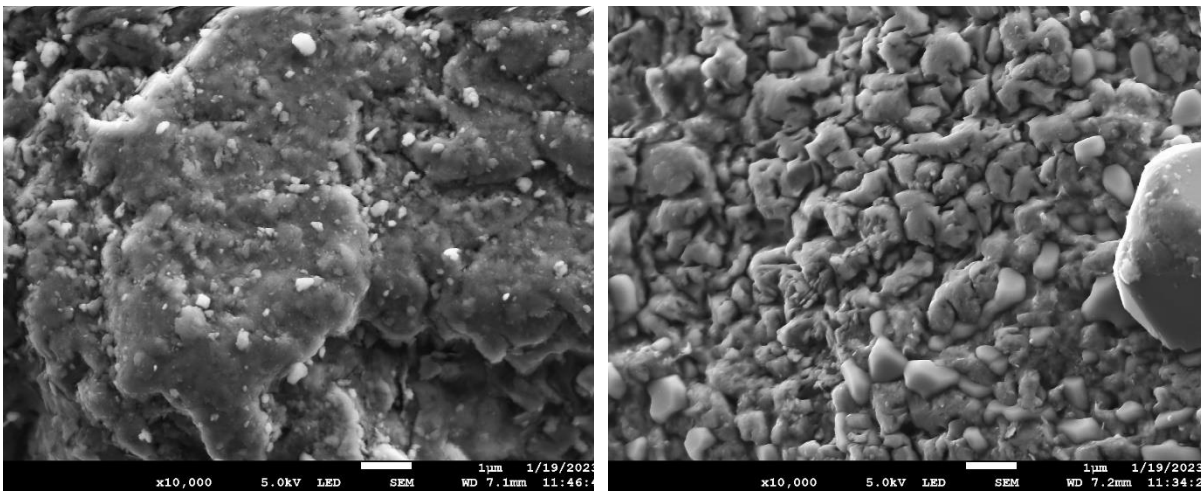

Figure 15: SEM images of unexposed (left) and exposed (right) silica.

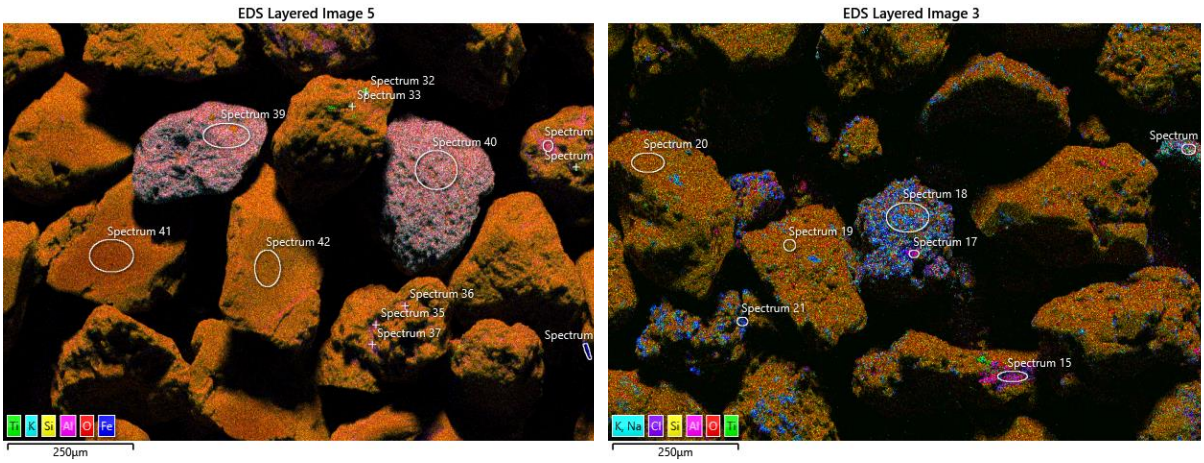

Figure 16: EDS maps of unexposed (left) and exposed (right) silica. Quantification of shown regions are given in the tables below (Table 2 and Table 3).

Table 2: EDS quantification of unexposed silica. Lines in the table have been given colours to help navigate in the EDS maps. All values are in at%.

Label	O	Na	Mg	Al	Si	K	Ti	Cr	Fe
Map Sum	69.4	0.1		1.7	27.5	1.1	0.1		0.1
48	20.7				10.8			9.9	58.6
32	72.0			0.8	4.4	0.1	22.7		
33	67.6			1.4	8.1	0.2	22.5		0.2
34	69.6			0.8	12.3	0.2	16.8		0.2
35	64.9	0.1	0.2	12.8	19.5	2.5			0.2
36	70.9	0.1	0.4	6.4	20.7	1.1			0.4
37	65.6	0.1	0.2	10.4	21.5	2.1			0.3
38	68.2	0.2	0.3	8.4	20.6	1.3	0.5		0.5
39	69.7	0.5		6.1	19.4	4.3			
40	66.2	0.4		6.5	22.0	4.9			
41	78.4			0.3	21.3				
42	71.8			0.3	27.9				

Table 3: EDS quantification of exposed silica. Lines in the table have been given colours to help navigate in the EDS maps. All values are in at%.

Label	O	Na	Al	Si	Cl	K	Ti	Fe	Ni	Cu
Map Sum	64.0	4.0	1.0	27.5	2.9	0.3	0.1	0.1	0.2	
15	55.7	7.2	11.8	16.8	4.5	1.8		1.0	1.2	
16	63.1	3.6	6.7	19.3	2.0	5.4				
17	36.6	8.6	28.2	15.1	8.3	1.7			0.7	0.9
18	49.1	15.6	3.0	18.5	11.7	1.9			0.2	
19	72.0	0.5		27.4	0.2					
20	72.5	0.5	0.2	26.6	0.3					
21	29.1	29.5	0.6	12.8	27.7			0.2	0.0	

2.4 CONCLUDING REMARKS

In this study an experimental setup for investigating mineral solubility at high salinity conditions was designed and tested. The setup was further used to perform experiments to study silica solubility and kinetics in the temperature range 100 to 200°C and NaCl concentration range 50.92 to 338.09 g/kg H_2O. Two types of experiments were performed, one to study silica solubility at equilibrium conditions and one to study solubility kinetics. The aim of the study is to increase the knowledge of solubility and precipitation of silica at high saline conditions.

The main findings from the equilibrium solubility study are that silica solubility increases with temperature and decreases with salinity. Results from the kinetic experiments corresponds well with the results from the study performed at equilibrium conditions. However, as for the equilibrium results, the results obtained matches with values for amorphous silica (see chapter 4.4), not quartz as expected from initial XRD measurements. No proper explanation is currently available. However, unidentified impurities are observed when the silica was characterised. This is not unusual for natural samples and might have influenced the solubility.

Ideally, results from solubility experiments should be compared with results from precipitation experiments to validate the transition state assumption outlined in the introduction. It was, however, not possible to include this within the current project. For future work experiments studying direct precipitation should be performed. In addition, the experimental matrix should be extended to kinetic solubility experiments covering more temperatures and salinities.

3 TASK 2.3.2 - MINERAL PRECIPITATION BY IMPEDANCE SPECTROSCOPY

3.1 INTRODUCTION

Scaling is one of the major obstacles for an economically efficient utilization of geothermal energy, as it often causes frequently and costly maintenance of both subsurface and surface installations including production and injection wells, pumps, and heat exchangers (e.g. Wanner et al., 2017, Köhl et al, 2020). Commonly, geothermal fluids contain a multitude of dissolved components such as salts, minerals and gases. However, changes in pressure and temperature during fluid extraction for geothermal energy and power production disturb the hydro-chemical equilibrium and may lead to mineral precipitation due to supersaturation, what in consequence can significantly reduce the flow rates of the geothermal system and rise the economic risk (e.g. Atkinson et al., 1991).

Calcite is one of the most abundant scaling minerals and can be found across a variety of geothermal production sites (Arnórsson, 1981; Haklidir and Balaban, 2019). Calcite is widespread in geothermal reservoir rocks, which is why in-situ formation waters are generally calcite saturated (Arnórsson, 1981). Carbonate scaling is mainly associated with CO_2(aq) degassing from the geothermal fluid due to decompression and a subsequent increase in pH, which significantly reduces the solubility of carbonate minerals. Generally, the potential of calcite supersaturation is largely controlled by the initial temperature, the initial CO_2 partial pressure (pH), and salinity of the formation water, and is highest when pH and salinity are highest and temperature is lowest (Arnórsson, 1989). Accordingly, calcite scaling is rampant in low (80 – 120 °C) to medium (130 – 200 °C) temperature sites (Wanner et al., 2017; Quinao et al., 2017), but also causes serious problems in some high-temperature geothermal fields with temperatures of up to 250 °C (Li, 2017). Thus, precise knowledge of hydro-chemical solution equilibria provides an important tool that can be used to prevent unwanted mineral precipitation by adjusting operational production conditions.

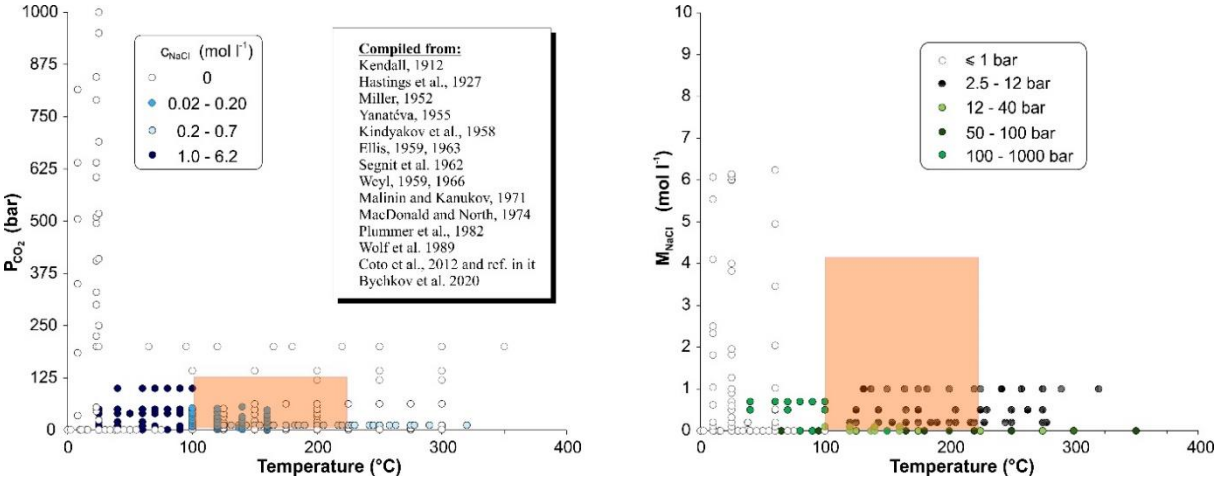

Figure 17: Compilation of available calcite solubility data, measured in dependence of temperature, pressure, and salinity of the solvent. For comparison, the red area marks relevant conditions of geothermal fluids in terms of salinity and temperature.

Calcite solubilities in water and brines up to 6 M NaCl have been widely studied experimentally at temperatures below 100 °C (Kendall, 1912; Hastings et al., 1927; Miller, 1952; Yanatéva, 1955; Kindyakov et al., 1958; Weyl, 1959, 1966; MacDonald and North, 1974; Plummer et al., 1982, Wolf et al. 1989; Coto et al., 2012 and ref. in it), though a large number of the published data only cover ambient temperature and pressure conditions (Figure 17). Only limited experimental data are available for temperatures up to 300 °C and CO_2 pressures between 1 – 150 bar (Ellis, 1959, 1963; Segnit et al. 1962; Malinin and Kanukov, 1971; Bychkov et al. 2020), and there is a general lack for calcite solubility in high-salinity brines (>6 wt% NaCl). As a consequence, large uncertainties in current model predictions arise. In order to better predict the scaling behavior of highly saline geothermal fluids in geotechnical installations, new solubility experiments were performed, focusing on fluids with salinities of 35 – 200 g/l NaCl, which are typical for most mid European geothermal sites. Here, we present results from a series of systematic measurements targeting a temperature range of 24 – 210 °C at CO_2 pressures between 1 – 50 bar. We use in-situ electrical impedance spectroscopy to define equilibrium conditions in the test solutions.

3.2 EXPERIMENTAL

3.2.1 Development of a high-temperature conductivity probe

The solubility of calcite is highly influenced by the amount of carbonic acid present in the solution and already small fluctuations in pressure and temperature have an immediate effect on its pH. In order to keep system disturbances during the experiments to a minimum, the dissolution/precipitation process was continuously monitored by electrical conductometry. For this, a 4-point electrode system was developed, which had to be capable for electrical conductivity measurements at elevated temperature and pressure. The conductivity probe consists of a rod-like corpus made of PEEK, to which lower end two Ag/AgCl plates (current electrodes) are attached vis-a-vis and supernatant with a defined electrode spacing (Figure 18). Two additionally Ag/AgCl wires, placed between the current electrodes, serve as potential electrodes and are sealed into the corpus. An O-ring sealed adapter was designed for the dimensions of commercial high-pressure screw-in drivers, and is provided for the pressure-

tight attachment in the lid of the autoclave. The conductivity probe was used up to 213 °C and a system pressure of 70 bar.

For conductivity measurements, an impedance spectrometer (Zahner-Zennium electrochemical work-station) was used to apply an AC voltage of 50 mV to the current electrodes. The conductance bridge provides the impedance, Z, and phase angle, ϕ, at distinct frequencies. The conductivity of the test solution, σ_{fl}, is given by

$$\sigma_{fl} = c/R, \tag{1}$$

with R is the sample resistance, derived from

$$R = cos\varphi \cdot Z, \tag{2}$$

and c is the cell constant, which considers the geometry of the electrode layout. The cell constant of the conductivity probe was experimentally determined using distilled water, tap

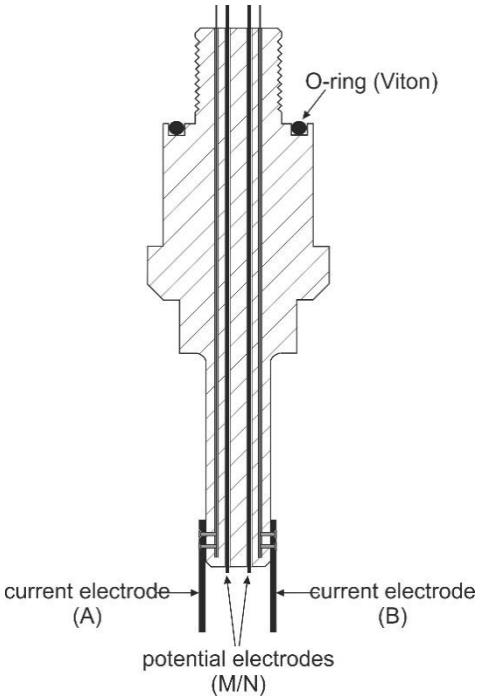

Figure 18: Schematic illustration of the high-temperature conductivity probe.

water, as well as 0.01 M and 0.1 M NaCl solutions at ambient conditions. Variations in the electrode spacing due to thermal expansion is regarded to be < 1 % at 200 °C, leading to an overall underestimation of σ_{fl} by 3% at maximum temperature.

The high-temperature electrode works well over the entire temperature range in solutions of with a concentration of up to 10 wt% NaCl ($\sigma_{fl\,(23°C)}$ = 73 mS/cm), whereas the measurements in the 20 wt% NaCl solutions ($\sigma_{fl\,(23°C)}$ = 223 mS/cm) had to be stopped at temperatures above 100 °C, since the signals become too low impedance at high temperatures and are then not resolvable with the used impedance spectrometer.

3.2.2 Materials

The solubility of calcite has been determined in pure water and NaCl solutions with concentrations of 5 wt%, 10 wt%, and 20 wt%. The sodium chloride solutions were made from high-purity NaCl and degassed deionised water. For the solubility tests, predominantly an ultra-pure, commercial calcite powder (Merck/ particle size = 10 µm) was used. Solubilities in a 5 wt% NaCl solution were determined both for the Merck-calcite as well as a natural Iceland spar. Purity of the Iceland spar was controlled by RFA analysis. It was found that impurities of Fe, Mg, and Mn are present only in traces (Table 4). For the experiments, the Iceland spar was crushed and subsequently fractionated into grain size classes by dry sieving, whereby primarily, the particle fraction 46 - 120 µm was used in the tests. It was washed with deionised water until the filtrate was clear and then treated with 0.01M HCl for 10 seconds to remove remaining micro-particles, before the calcite powder was rinsed again with deionised water and finally vacuum-dried for 24 hours at 60 °C.

Table 4: RFA analysis for the Iceland spar.

CaO (%)	MgO (%)	Fe_2O_3 (%)	MnO (%)
51.58	0.16	0.33	0.13

The determination of the mineral surfaces using the BET gas adsorption method was only possible for the pure calcite (84500 cm^2/g), since the resolution limit of the available device was exceeded for coarser grain fractions. Thus, for the grain fraction 45-125 µm, the surface area had to be calculated from mineral geometries. However, steps and other irregularities of the surface are not considered, which is why the mean surface area of 133 cm^2/g is regarded a minimum estimate.

3.2.3 Experimental setups and methods

3.2.3.1 Procedures for the determination of calcite solubilities

Calcite solubility experiments at elevated temperature and pressure were conducted in two stainless steel batch reactors with a total capacity of 900 ml (Figure 19). To avoid corrosion, the reactors are lined with beakers made of Teflon or silica glass, respectively. The beakers were filled with 800 g of the solvent into which 10 to 40 g of calcite powder was weighed out. The amount of calcite material used exceeded the solubility by more than 10 times in all experiments, thus, a constant particle surface was assumed. During the experiment, the solutions were stirred by a magnetic stirrer at a continuous rate of 350 rpm. Calcite solubilities were determined at equilibrium between 24 – 210 °C and 1 – 50 bar pCO_2, defined as the difference of the absolute pressure in the autoclave and the vapour pressure of water at the particular temperature. At equilibrium conditions, Ca^{2+} concentrations, $[Ca^{2+}]$, were determined via complexometric titration with EDTA at pH 10, whereby the titration end point is colour-indicated by Eriochrome Black T. The determined $[Ca^{2+}]$ is based on the mean values of 5 individual titrations with an analytical uncertainty usually below 1 %.

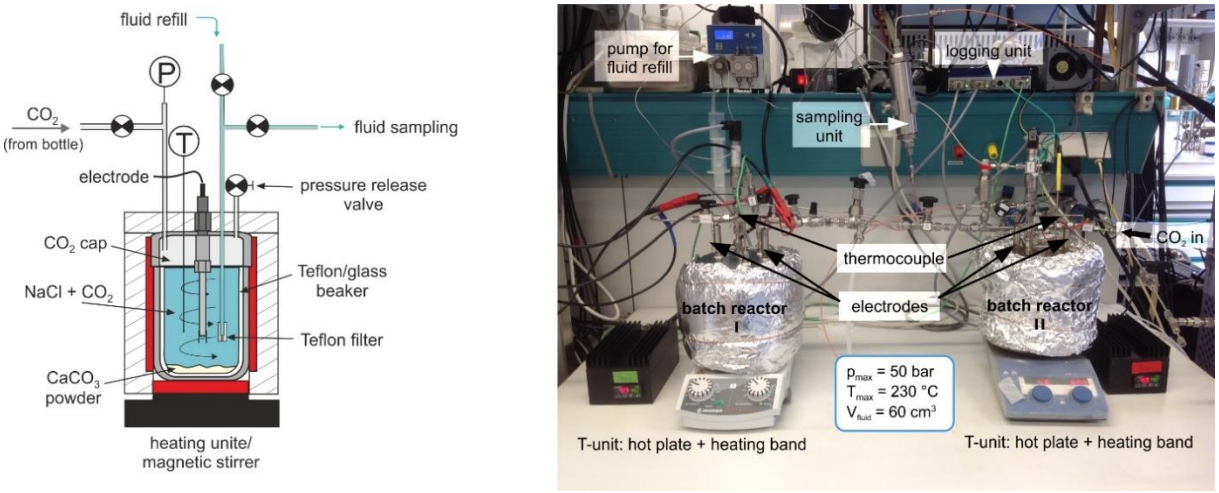

Figure 19: Experimental set-up (left) and a schematic overview of the batch reactor (right) used in solubility/ precipitation experiments of calcite.

For pressurization, both autoclaves were connected to a CO_2 bottle, whereby the system pressure was regulated via a pressure reducing valve at the bottle and metering valves at the autoclaves. Autoclave pressures were monitored by high-precision, dead-weight calibrated sensors with an accuracy of ±0.2 bar. Before the experiment, CO_2 was flushed for approximately 15 - 20 min through the gas cap volume of the autoclaves to remove air from the vessels via open pressure release valves, which were closed afterwards to apply the desired pressure. For temperature control, the autoclaves were placed on heating plates /magnetic stirrers and jacketed with thermally-insulated heating sleeves, so that essentially the whole vessel including the gas cap was at constant temperature. The heating-sleeves were connected to controllers to keep the temperature constant ±0.1 °C. The fluid temperatures were monitored by K-type thermocouples, placed in Teflon coated, dead-ended Hastelloy capillaries, which again were directly immersed in the tested solutions.

The achievement of equilibration between solution and calcite powder at the desired pressure and temperature conditions was determined via continuous electrical impedance measurements. When changes in the electrical impedance were less than 1 % for 12 hours, solubility equilibrium was assumed and fluid samples were extracted at system pressure and temperature through a PEEK capillary with attached 2 µm Teflon filter. To avoid contamination, the sampling capillary was flushed with about 10 ml of the produced fluid, which was poured away, before the proper sample was taken. To check for consistency, 1 to 3 further aliquots were taken in time intervals of 4 hours up to 24 hours and analyzed with EDTA titration.

Samples, taken at temperatures below 100 °C, were discharged directly into a tube, containing a weighted amount of bi-distilled water to avoid precipitation, when the pressure was released to atmospheric conditions. In total, a maximum sample volume of ca. 350 cm^3 could be extracted from the vessel, before the electrodes became partially exposed. Therefore, several fluid samples could be taken from the test solutions at different temperature and pressure levels, before the vessel had to be recharged.

3.2.3.2 Procedure for kinetic experiments

Kinetic experiments on calcite precipitation were run with two different approaches. In the classic approach, fluid samples were taken at defined time intervals from the batch reactors and analysed for $[Ca^{2+}]$ by complexometric EDTA-titration. The minimum time interval was 4 minutes. Additionally, the electrical impedance was logged (Figure 20), which shows a linear

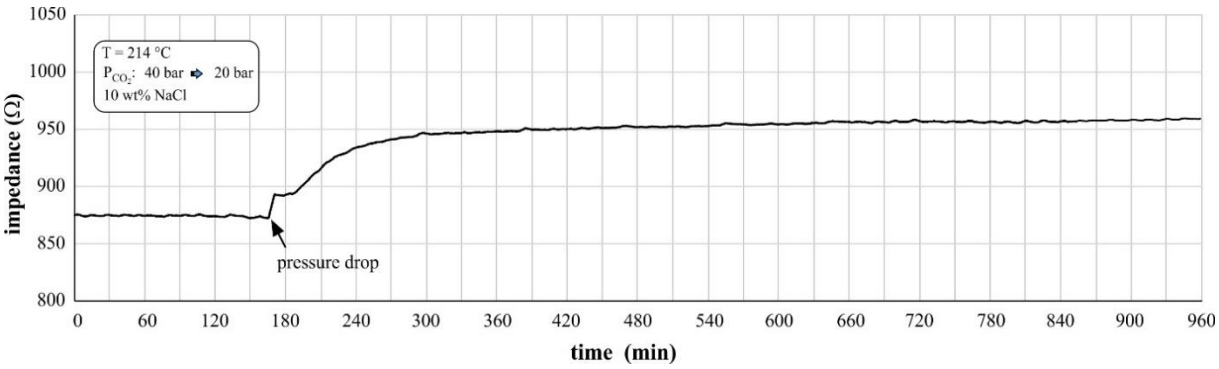

Figure 20: Impedance log of a kinetic $CaCO_3$ precipitation experiment.

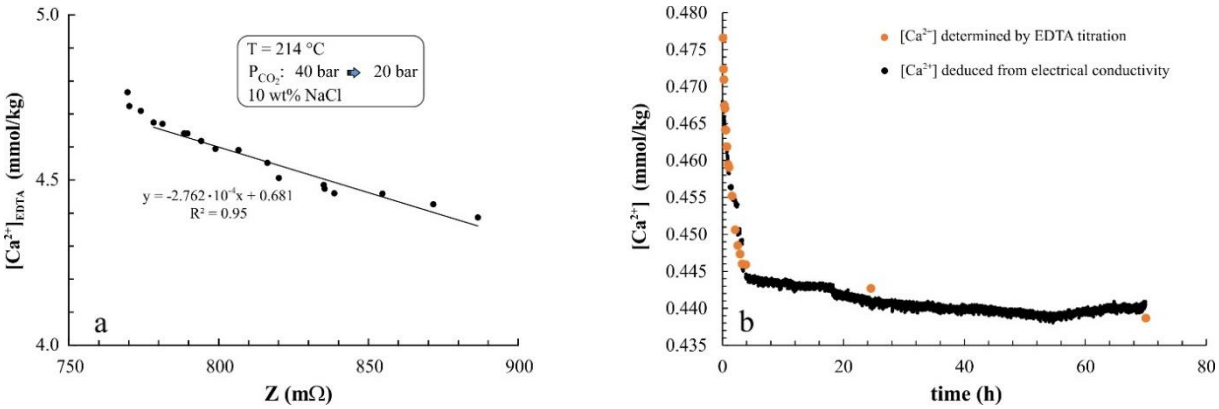

Figure 21: (a) $[Ca^{2+}]$ determined from EDTA titration vs. electrical impedance. (b) Comparison of $[Ca^{2+}]$ deduced via EDTA-titration and via conductometry, respectively.

relationship with titrated $[Ca^{2+}]$ (Figure 21a). Thus, the measured conductivity can be used as a measure for the Ca^{2+} concentration (Baumann et al., 1985, Dreybrodt et al., 1996, Vosbeck, 2004). Since only one impedance spectrometer was available and therefore the autoclaves could not be monitored in parallel by electrical measurements, both methods were used throughout the entire study. Beyond this, for the experiments with 20 wt% NaCl solutions the electric measurements had to be terminated prematurely at 100 °C, due to extremely low impedance.

Kinetic experiments were performed in the systems H_2O – $CaCO_3$ and H_2O – NaCl - $CaCO_3$, whereby the calcite substrate contained either 100 % $CaCO_{3(Merck)}$ (mean grain size = 10 µm), or 90 % $CaCO_{3(Merck)}$ + 10 % $CaCO_{3(Iceland\ spar)}$ (particle size fraction: 45-125 µm), 90 % $CaCO_{3(Merck)}$ + 10 % $CaCO_{3(Iceland\ spar)}$ (125-185 µm), and 100 % $CaCO_{3(Iceland\ spar)}$ (45-125 µm), respectively. The loading of the autoclaves and setting the pressure and temperature conditions followed the same procedures as described for the solubility experiments. A kinetic experiment was

started when the system was in equilibrium (approximately 4 to 6 days after adjusting the pT conditions). For better comparability of the kinetic tests, both autoclaves were operated in parallel whenever possible, with the gas caps in both autoclaves being short-circuited via an open valve in order to ensure the same pressure conditions in both containers.

3.3 RESULTS AND DISCUSSION

3.3.1 Equilibrium experiments

The solubility of calcite has been tested in pure water and NaCl solutions with concentrations of 5 wt%, 10 wt%, and 20 wt%. The measurements were conducted in a temperature range of 24 – 210 °C and covering CO_2 pressures of 1 – 50 bar. The results are plotted in Figure 22 as function of temperature and pCO_2. In all tested solvents, the solubility of calcite decreases exponentially with increasing temperature and constant pressure, while the solubility increases with increasing pCO_2 at isothermal conditions. However, the pressure effect diminishes with increasing temperature as the solubility values converge and nearly equal at temperatures above 200 °C. Solubilities were predominantly determined by using ultra-pure calcite. However, for solubility tests in 5 wt% NaCl solution ultra-pure calcite and natural Iceland spar, respectively, were used for comparison in parallel runs. It was found that variations in solubilities of both materials were lower 1 %.

Where available, the data of this study agree with data from previous studies (Miller, 1952; Ellis, 1959, 1963; Segnit, 1962; Bychkov et al., 2020). An extensive data set is available for calcite solubility in water (Miller, 1952; Signet, 1962; Ellis, 1963). Figure 23 summarises these literature data and corresponding results of this study.

Figure 24 depicts the variation of calcite solubility in dependence of NaCl concentration for two temperatures. For comparison, data measured at 10 bar in this study were checked against data from Ellis (1963), which were determined at comparable pressure and temperature conditions. The agreement between the two datasets is reasonably satisfactory. The solubility of $CaCO_3$ shows a maximum between 5 to 10 wt% NaCl (0.8 - 1.7 mol/l NaCl) in the solution and decreases again at higher salinities. This observation is consistent with modeling results by Coto et al., 2012, who found the maximum solubility of calcite in a $CaCO_3$ - NaCl - H_2O system at a molality of about 1.25 mol cm^{-3} (7.3 wt% NaCl).

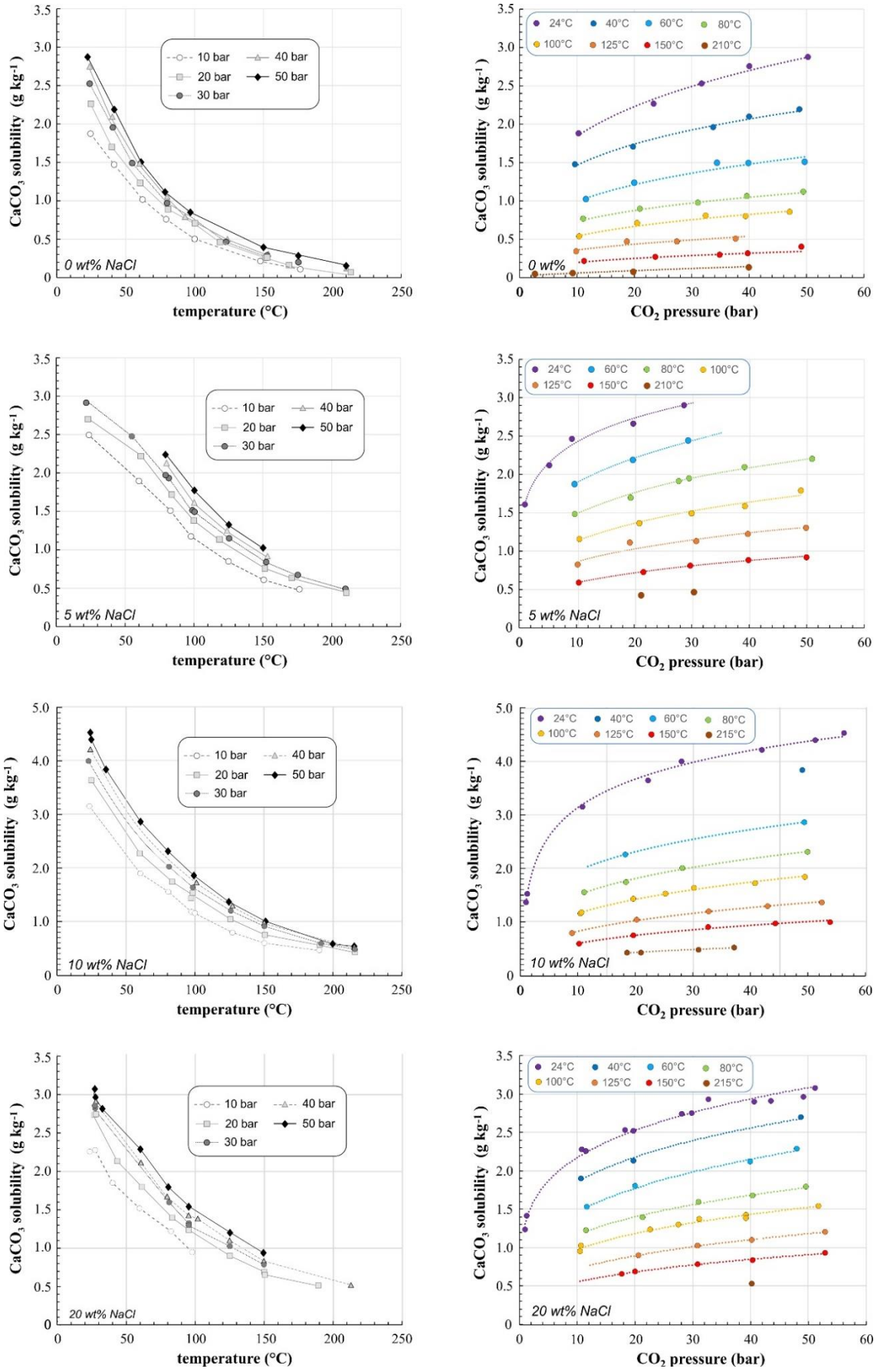

Figure 22: Solubility of calcite in dependence of temperature, CO_2 pressure, and fluid salinity.

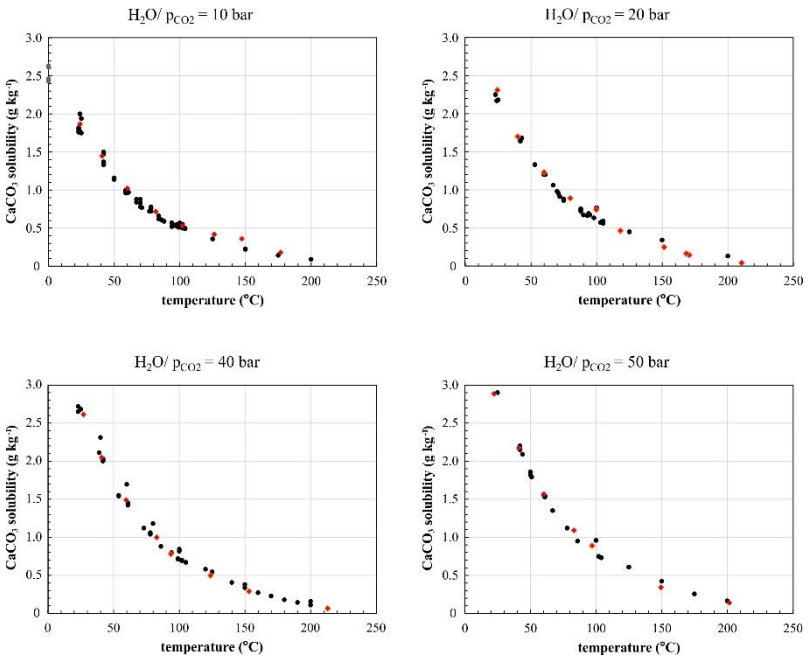

Figure 23: Calcite solubilities ($CaCO_{3(Merck)}$) in pure H_2O at different CO_2 pressure levels of this study (red dots) are found to be in remarkable agreement with available data of Miller,1952, Segnit,, 1962, and Ellis, 1963 (black dots), who measured on natural calcites.

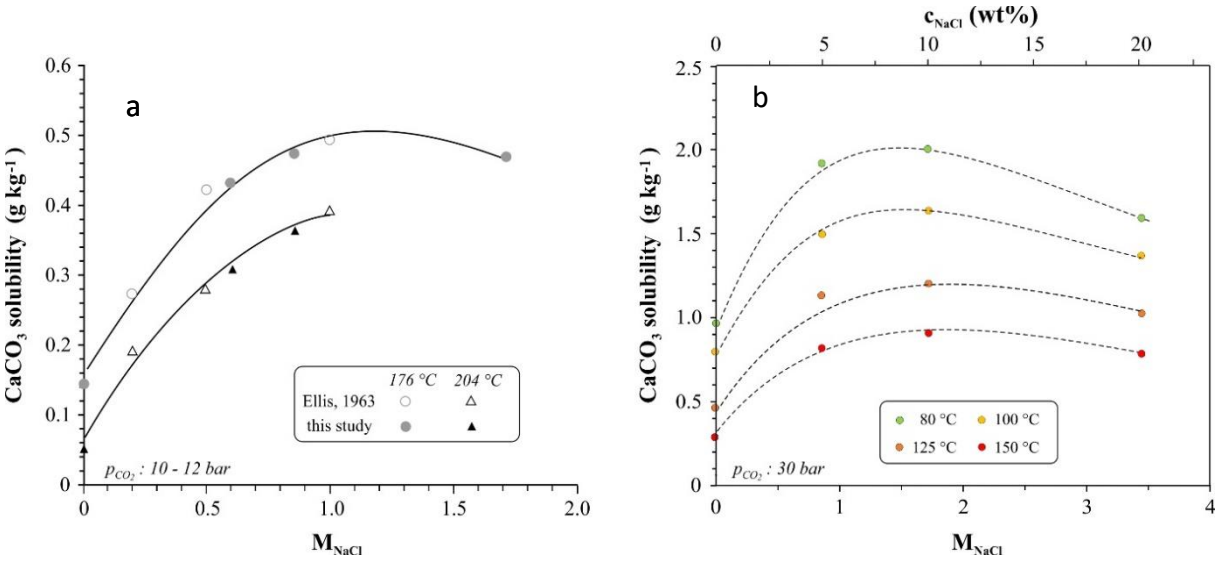

Figure 24: Effect of NaCl on calcite solubility as function of fluid salinity at p_{CO2} of 12 bar (a) and 30 bar (b), respectively.

3.3.2 Kinetic experiments

Carbonate scaling in geothermal installations is mainly associated with $CO_{2(aq)}$, degassing from the geothermal fluid due to production-related decompression and a subsequent increase in pH. Therefore, kinetic experiments were performed at constant temperature and stirring rates, but simulating a pressure drop in the system (Figure 26).

For a better comparison of the different experiments, relative saturations, c_{rel}, were calculated from:

$$c_{rel} = \frac{c - c_{eq}}{c_0 - c_{eq}}, \quad (3)$$

with c is the actual concentration of $[Ca^{2+}]$, c_0 is $[Ca^{2+}]$ at the beginning of the kinetic experiment (excess concentration), and c_{eq} denotes the equilibrium concentration for the given pressure and temperature conditions.

Though experiments with 10 wt% NaCl and 20 wt% NaCl were run at identical regarding temperature, pressure, decompression rate (R_{decomp}), stirring rate, and composition of the calcite substrate (20 g Merck-Calcite [10 µm] + 2 g Iceland spar [45 - 125 µm]), after about 35 min an offset in relative saturation developed and equilibrium conditions where reached faster in the 20 wt% NaCl solution than in the 10 wt% NaCl solution (Figure 25a). Usually, after 4 to 6 days equilibrium concentrations reached in the kinetic experiments correspond well with the equilibrium concentrations found in the solubility experiments, whereby the elapsed time decreases with increasing temperature. For precipitation in a 5wt% NaCl solution a steeper exponential decrease in relative Ca^{2+} saturation was observed. This is probably due to the fact that the calcite substrate here consisted of 100% Iceland spar with grain size fraction of 45 – 125 µm. After about 60 min, c_{rel} match with those obtained in the 20 wt% NaCl solution. Fast R_{decomp} seem to induce a steep decline in $[Ca^{2+}]$, while a slow pressure drop results in a more gradual decrease in $[Ca^{2+}]$ (Figure 25b). Also, high R_{decomp} in combination with enhanced Ca^{2+} availability in saline fluids seem to hamper the equilibration of the system and to elongate the duration of oversaturated conditions. Moreover, larger seed crystals accelerate precipitation kinetics (Figure 25c and d).

The dissolution rate, R in mmol/(cm^{2}s), was calculated by numerical differentiation of the $[Ca^{2+}](t)$ curve :

$$R = \frac{V}{A} \cdot \frac{d[Ca^{2+}]}{dt}, \quad (4)$$

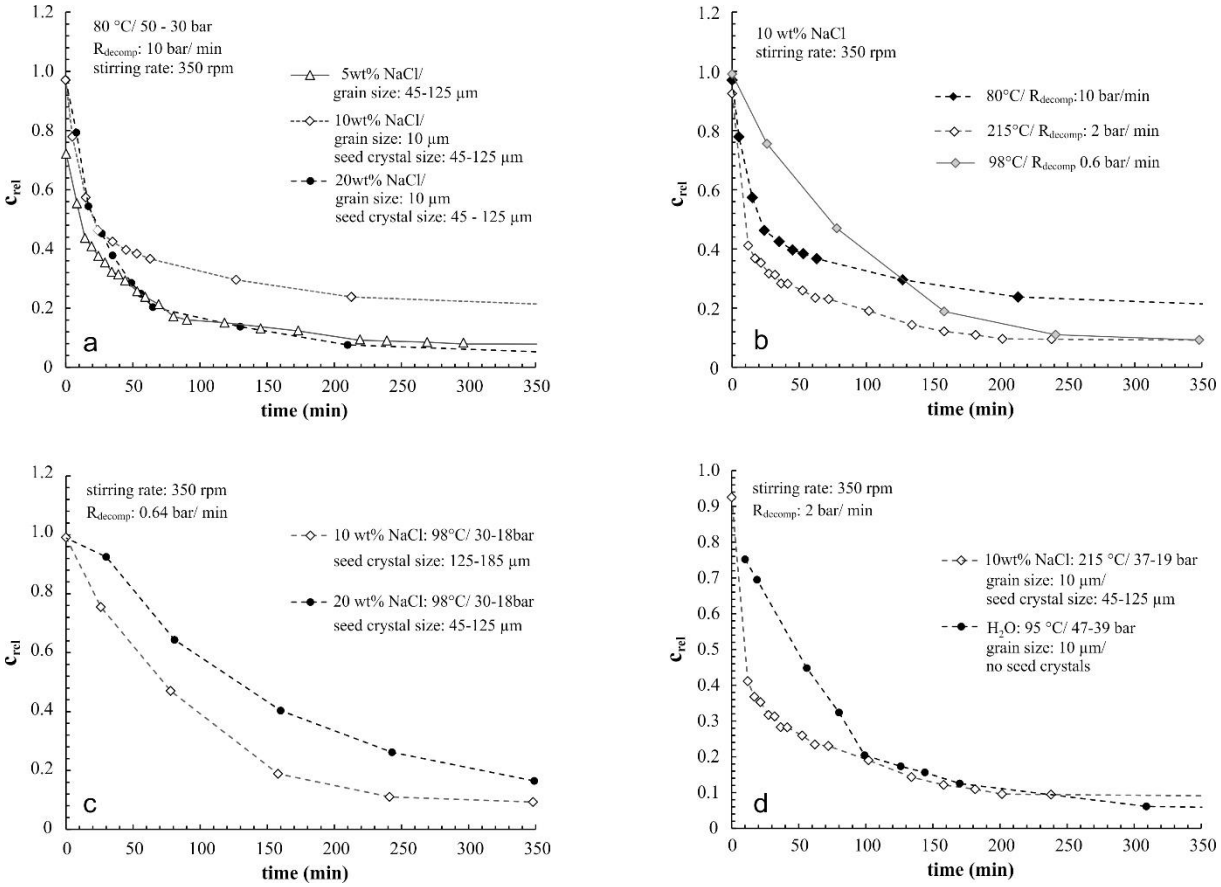

Figure 25: Results for kinetic calcite precipitation experiments obtained for various fluid salinities, temperatures, and grain size fractions. For a better comparison of the different experiments, [Ca^{2+}] is given as relative saturations, c_{rel}. (Abbrevations: R_{decomp} = decompression rate, rpm = repeats per minute.)

where *V* and *A* are the solution volume and effective mineral surface, respectively and the term $d[Ca^{2+}]/dt$ denotes the changes in [Ca^{2+}] in dependence of time.

Figure 26 shows log-log plots of the precipitation rate versus relative Ca^{2+} saturation for fast and slow CO_2 pressure drop, respectively. Slopes in the range of 1.01 - 1.16 indicate first-order reactions. However, for fast decompression the change in slope of the function points to a change in precipitation kinetics. In particular, such behavior was described for studies with natural limestone at ambient conditions (Plummer and Wiley, 1976; Svensson and Dreybrodt, 1992; Eisenlohr et al., 1999, Vosbeck, 2004).

For a final evaluation of the kinetic data we lack further SEM analyses, which are not available yet, due to a severe average in the GFZ electrons microscopy laboratory.

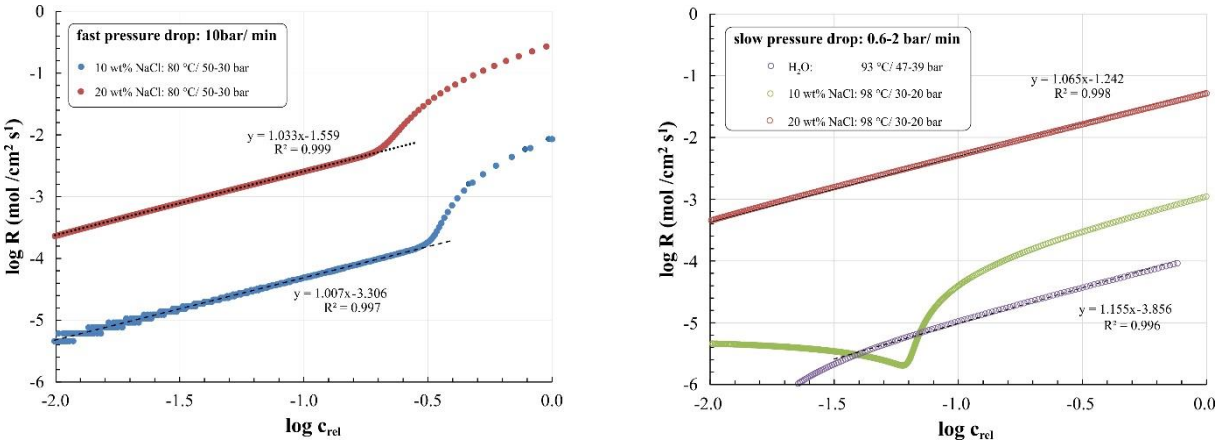

Figure 26: Log-log plots of precipitation rate vs. relative Ca^{2+} saturation for fast and slow decompression rates.

3.4 CONCLUDING REMARKS

Precise knowledge of hydrochemical solution equilibria provides a tool that can be used to prevent unwanted mineral precipitation by adjusting operational production conditions. The extensive equilibrium measurements carried out in this study, thus, contribute to a general broadening of the existing experimental database, suitable to finally calculate solubility products and stability constants of aqueous calcium carbonate and bicarbonate complexes at elevated pressure and temperature conditions.

The system $CaCO_3$ - H_20 - NaCl - CO_2 is complex, and the relationships that control the precipitation reactions are correspondingly complex. Due to the lack of time caused by the pandemic, kinetic experiments could only be carried out to a limited extent, so that known influencing variables such as the flow rate (stirring rate) were not taken into account in this study. In order to develop a more precise understanding of the precipitation rates of calcite in hot, highly saline water, this work should be continued elsewhere with the aim of systematically examining the influence of flow rates, temperature, and salinity on calcite precipitation.

4 TASK 2.3.3 - A KINETIC MODEL OF SILICA PRECIPITATION AND DISSOLUTION

4.1 INTRODUCTION

Silica precipitation is one of the main technical issues that geothermal plants have to deal with. Indeed, silica has a retrograde behaviour, which means that its solubility decreases with decreasing temperature. Thus, in a number of geothermal plants, pumped hot waters are characterized by high silica contents and, after heat has been extracted, these cooled waters are supersaturated with respect to silica. Depending on various parameters, silica precipitation risks can be dramatic for the surface installation of the geothermal plant or for the injectivity of reinjection wells. These parameters are, in particular, the production and

reinjection temperatures, the initial silica content, the chemistry of the brine including salinity and pH.

The kinetic rates of silica precipitation have been studied for several decades, with one of the first dedicated studies by Rimstidt and Barnes (1980) in deionised water for temperatures between 25 and 300°C. These authors proposed a simple kinetic law based on the transition state theory (Eyring, 1935; Lasaga, 1981) and considering several influencing factors:

- temperature;
- the ratio of the relative interfacial area between the solid and aqueous phases over the relative mass of water in the system;
- the activity coefficient of the H_4SiO_4 aqueous species;
- activities of water and solid silica.

Later, Dove and Icenhower (1997) pointed out the catalysing effect of simple dissolved elements on the precipitation rate of silica. More recently, Dixit et al. (2016) showed experimentally that, in addition to temperature, pH plays a significant role on the precipitation rate of silica, at least in the specific context of the geothermal waters of Bouillante, Gadeloupe. The role of pH was further demonstrated by André et al. (2017) as they studied more specifically the surface state of silica grains. They developed a surface complexation model to describe protonation reactions of silanol sites outcropping of silica surface. Such reactions affect the surface charge of the grains as a function of pH. In presence of dissolved magnesium, the surface charge influences the capacity of magnesium complexation at the surface of the grain and thus its catalysing property on silica precipitation rate.

Amongst the mechanisms that promote the precipitation rate of silica is the seeding of the aqueous solution with solid particles, like silica gel seeds (Setiawan et al., 2019). The goal is to introduce in the solution surfaces from which solid silica can grow by minimizing the energy of nucleation required in the case of homogeneous nucleation. However, this option will not be considered in the following and focus is made on spontaneous formation of silica from aqueous solution.

Actually, very few published works report comprehensive experimental data about the kinetics of silica precipitation from aqueous solutions. A series of two papers (Conrad et al., 2007; Icopini et al., 2005) are considered as references in this domain. However, in the kinetic law proposed by Conrad et al. (2007), parameters k_1 and k_2 were determined independently for each condition of pH, salinity and initial concentration of dissolved SiO_2. This limits somehow the use of this law. Dixit et al. (2016) also proposed a kinetic law for silica precipitation from the geothermal waters of Bouillante. This law, based on the TST and inspired by the model of Icopini et al. (2005), includes a pH dependence but different parameters were developed for each studied temperature.

The objective of the present work was to propose a single kinetic law for silica precipitation that can overcome these limitations.

4.2 METHODOLOGY

The experimental observations by Icopini et al. (2005) show that silica precipitation occurs as a two-step process. It includes the preliminary formation of nano-sized particles, which are replaced progressively by larger silica precipitates. Accordingly, these authors proposed a combination of two kinetic laws in order to describe the evolution of the dissolved monomeric silica and that of nanocolloidal silica particles with time. Then, Conrad et al. (2007) improved the model by introducing a supersaturation condition so that the kinetics slow down when the system approaches equilibrium.

It should be noted here that the two-step process of silica formation from the aqueous solution observed by Icopini et al. (2005) is not an exception. Indeed, such a process has been observed in several other chemical systems like $BaSO_4$-H_2O (Ruiz-Agudo et al., 2020), $CaPO_4$-H_2O (Jiang et al., 2015), $CaSO_4$-H_2O (Van Driessche et al., 2012), (Ca-Mg-Fe)CO_3-H_2O (Dideriksen et al., 2015; Forbes et al., 2011; Radha et al., 2012, 2010; Sel et al., 2012). This led Ruiz-Agudo et al. (2020) to conclude that this type of two-step process is more the rule than the exception. It has also been modelled successfully in the $CaCO_3$-H_2O system, considering the relative stability of the amorphous and the crystallized particles, as well as their surface reactivity (Lassin et al., 2018).

In the present work, it is proposed to develop a new model based on that of Conrad et al. (2007), and using the experimental data acquired by Icopini et al. (2005). The following experimental conditions were considered by the authors, and are also considered in the present study:

- Initial SiO_2 content = 4.2, 12.5 and 20.8 $mmol \cdot kg^{-1}$,
- pH = 3, 4, 5, 6, 7,
- Ionic strength = 0.01, 0.24 $mol \cdot kg^{-1}$ imposed using a stock solution made of 200 millimolal Na^+, 25.1 millimolal K^+, 5.00 millimolal Ca^{2+}, 236 millimolal Cl^-, and 0.739 millimolal HCO_3^-,
- Temperature = 25°C.

The two-step process to be modelled is schematically sketched in Figure 27. It includes the contributing elementary mechanisms like homogeneous nucleation, aggregation of nanocolloids, aging of nanocolloids, and mineral growth. Homogeneous nucleation is not considered explicitly in the proposed kinetic law but it could be considered by implementing an induction period before the appearance of nanocolloids.

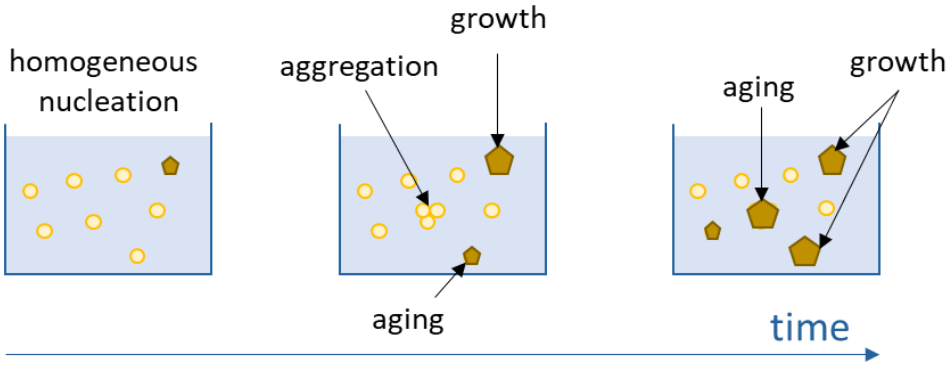

Figure 27: Sketch of the two-step process described by the proposed kinetic model. Yellow circles represent nanocolloidal silica and brown pentagons represent amorphous silica precipitates.

Following the recommendations of Icopini et al. (2005) and Conrad et al. (2007), two kinetic laws are proposed to describe precipitation rates of nanocolloidal silica and of amorphous silica. The nucleation and growth mechanisms are represented by a term that obeys a 4th order trend with respect to monomeric dissolved silica and considers the supersaturation level of the solution with respect to solid amorphous silica. An additional term is implemented to reproduce the rate of transformation of nanocolloidal silica to precipitated amorphous silica with the aim to account for nanocolloidal silica aggregation and aging mechanisms. These two kinetic laws write as follows:

$$r_{SiO_{2(am)}} = \frac{dC_{SiO_{2(am)}}}{dt} = -\frac{k_1}{8} \times \left(SR_{SiO_{2(am)}} - 1\right)^4 - k_2 \times C_{SiO_{2(nano)}}^{2/3} \quad (1)$$

$$r_{SiO_{2(nano)}} = \frac{dC_{SiO_{2(nano)}}}{dt} = -\frac{7k_1}{8} \times \left(SR_{SiO_{2(am)}} - 1\right)^4 + k_2 \times C_{SiO_{2(nano)}}^{2/3} \quad (2)$$

r_i (in mol·s^{-1}), C_i (in moles), SR_i (unitless) are the rate of precipitation, the amount and the saturation ratio of compound *i*, respectively, where *i* denotes amorphous silica ($SiO_{2(am)}$) or nanocolloidal silica ($SiO_{2(nano)}$). k_1 and k_2 are two adjustable coefficients, k_1 being associated to the nucleation and growth terms, *i.e.* "**precipitation**", while k_2 being associated to the aggregation and aging terms, *i.e.* "**transformation**".

A factor 7 was found between the nucleation/growth rates of amorphous silica and of nanocolloidal silica, illustrating the faster nucleation of the latter. The second terms in the kinetic laws are exactly opposite to one another and illustrate the transformation of nanocolloidal silica to amorphous silica by aggregation and/or aging.

By means of the $SR_{SiO_{2(am)}}$ parameter, equations (1) and (2) are related to the dissolved silica concentration only. A pH dependency must be introduced in the k_1 and k_2 coefficients to take into account the sensitivity to acidity or basicity.
According to André et al. (2017), the surface charge of silica grains is almost 0 C·m^{-2} for pH below about 3.5 and becomes increasingly negative at higher pH values (Figure 28). It is expected that nanoparticle/nanoparticle and nanoparticle/dissolved species interactions increase with increasing pH. Nanoparticle/nanoparticle interactions are repulsive because of

their negative charge. On the contrary, nanoparticle-dissolved cations interactions are attractive. It is hypothesised that, in acidic to near-neutral pH conditions, there may be a competition between attractive and repulsive forces that could be in favour of aggregation. At higher pH, repulsive forces become predominant and hinder aggregation.

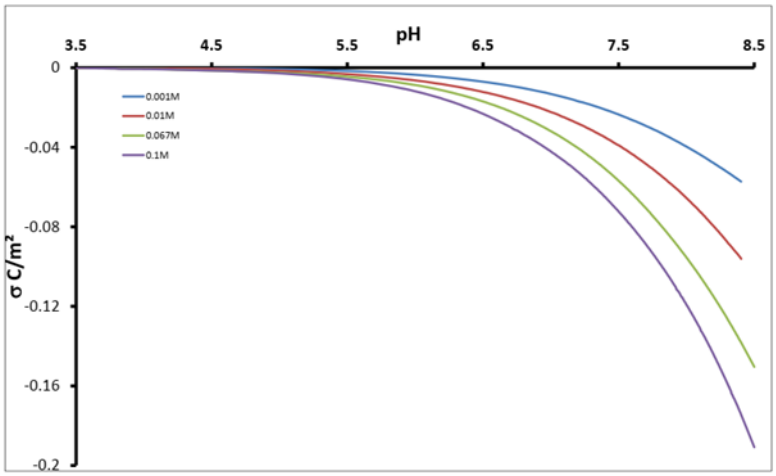

Figure 28: Surface charge of silica grains vs. pH in aqueous solutions with variable contents in $MgCl_2$ (between 0.001 and 0.1 molal), after André et al. (2017).

In the case of the low ionic strength solutions considered by Icopini et al. (2005), the log values of fitted k_1 and k_2 coefficients are plotted in Figure 29. They not only depend on pH, but also on the initial content of dissolved SiO_2.

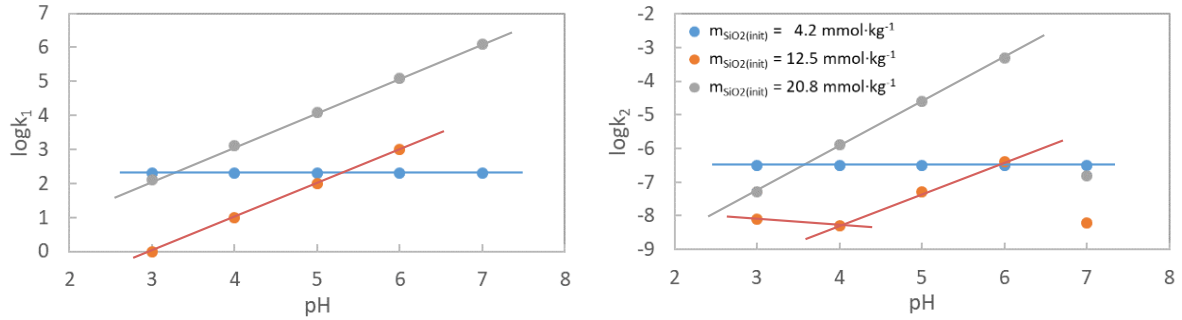

Figure 29: Fitted k_1 (nucleation/growth) and k_2 (aggregation/aging) coefficients vs. pH, for the kinetic laws (1) and (2), with different initial dissolved SiO_2 concentrations and a condition of low ionic strength (0.01 mol·kg^{-1}). Straight lines are a guide for the eye to illustrate linear domains of variation.

Observation of Figure 29 suggests that, depending on the initial content in dissolved SiO_2, the relative importance of aggregation and of aging varies within the transformation process (k_2). As mentioned previously, aggregation is expected to increase with increasing pH. Thus, it should be associated with the lines of positive slope. However, the right-hand side chart of Figure 29 shows that at pH 7, log k_2 sharply decreases at pH 7 (closed circles), suggesting that aggregation is not dominant any longer as inferred above. Conversely, aging is rather expected to be independent of pH and thus to be represented by a horizontal line. Moreover, it can also be expected that aggregation is favoured by the presence of numerous nanocolloidal silica particles, which is favoured by high initial dissolved SiO_2 contents.

Similar reflexions can be done regarding the nucleation/growth mechanisms within the precipitation process: nucleation is expected to be favoured by high initial dissolved SiO_2 contents and may vary with pH by means of the surface state of the nuclei. Conversely, mineral growth should be more inertial and less pH dependent.

These variations of the relative importance between the two types of mechanisms are sketched in Figure 30. At constant initial dissolved SiO_2, $m_{SiO_2}^{init}$, the logarithm of the kinetic coefficients k_1 and k_2 were found to be bilinear with respect to pH in the limited range where the nanoparticle/nanoparticle repulsive forces are not predominant. At constant pH, k_1 and k_2 were found to be bilinear with respect to the initial content of dissolved SiO_2, except for the second term of the k_1 coefficient. An additional second order term relative to $m_{SiO_2}^{init}$ was found necessary.

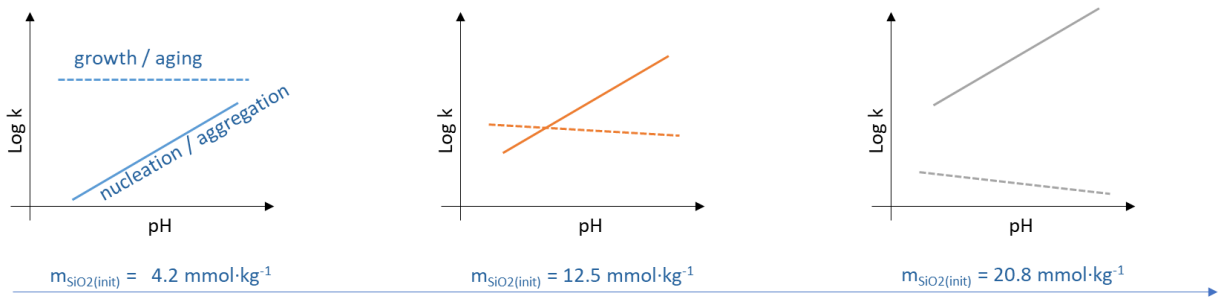

Figure 30: Sketch of the proposed relative evolution of the two types of mechanisms expected to rule the precipitation and transformation of nanocolloidal silica and of amorphous silica vs. pH and the initial dissolved SiO_2 content.

The mathematical representation of such behaviours is expressed as follows, for both k_1 and k_2 kinetic coefficients defined in equations (1) and (2):

$$k_i = 10^{\left[\left(a_{i,1}\times m_{SiO_2}^{init}+b_{i,1}\right)\times pH+\left(a_{i,2}\times m_{SiO_2}^{init}+b_{i,2}\right)\right]} + 10^{\left[\left(a_{i,3}\times m_{SiO_2}^{init}+b_{i,3}\right)\times pH+\left(a_{i,4}\times m_{SiO_2}^{init}+b_{i,4}+c_{i,4}\times\left(m_{SiO_2}^{init}\right)^2\right)\right]} \quad (3)$$

with i = 1 or 2.

In equation (3), the first term of the right member describes growth or aging mechanisms, and the second term describes nucleation/aggregation mechanisms. This equation is not ionic strength-dependent. Thus, the coefficients $a_{i,j}$ and $b_{i,j}$ (i = 1 or 2, j = 1 to 4) were fitted using data from Icopini et al. (2005) at 0.01 molal and 0.24 molal ionic strengths, separately. Then, assuming a monotonous dependency of these $a_{i,j}$ and $b_{i,j}$ coefficients with respect to ionic strength, additional simple relationships are proposed:

$$a_{i,1}(I) = p_{a,i,1}\ln(I) + q_{a,i,1} \quad (4)$$
$$b_{i,1}(I) = p_{b,i,1}\ln(I) + q_{b,i,1} \quad (5)$$
$$a_{i,j}(I) = p_{a,i,j}I + q_{a,i,j} \quad (6)$$
$$b_{i,j}(I) = p_{b,i,j}I + q_{b,i,j} \quad (7)$$
$$c_{i,4}(I) = p_{c,i,4}I + q_{c,i,4} \quad (8)$$

with i = 1 or 2, and j = 2, 3 or 4.

The p and m parameters involved in equations (4) to (8) were then determined by fitting the different values of $a_{i,j}$ and $b_{i,j}$ obtained for the two ionic strength conditions.

4.3 RESULTS

The parameters obtained for calculating the k_1 and k_2 kinetic coefficients of rate laws (1) and (2) are presented in Table 5. A total of 27 non-zero parameters were finally estimated. Application to the experimental conditions studied by Icopini et al. (2005) led to the graphical representations of Figure 31 for low ionic strength conditions (0.01 molal), and of Figure 32 for moderate ionic strength conditions (0.24 molal).

Table 5: Parameters necessary to calculate the k_1 and k_2 kinetic coefficients of rate laws (1) and (2).

	j	*1*	*2*	*3*	*4*
Main process	***Parameter***	***Growth***		***Nucleation***	
Precipitation	$p_{a,1,j}$	0	1.6737	0	1.3690
	$q_{a,1,j}$	0	-0.5349	0	0.2393
	$p_{b,1,j}$	0	-7.0293	0	-4.6250
	$q_{b,1,j}$	0	4.5477	1	-6.1164
	$p_{c,1,j}$	0	0	0	-0.06377
	$q_{c,1,j}$	0	0	0	0.000638
		Aging		***Aggregation***	
Transformation	$p_{a,2,j}$	0.026537	-0.3738	-0.55838	2.0652
	$q_{a,2,j}$	0.03787	0.0596	0.04434	0.1186
	$p_{b,2,j}$	-0.111457	1.57	10.422	-43.14
	$q_{b,2,j}$	-0.159062	-6.7503	0.4198	-13.724
	$p_{c,2,j}$	0	0	0	0
	$q_{c,2,j}$	0	0	0	0

The calculated evolution of dissolved monomeric silica, nanocolloidal silica and amorphous silica vs. time is plotted on charts that are superimposed for comparison on the figures taken from Conrad et al. (2007). There is a global match between the calculated concentrations and the experimental ones. In particular, the slow precipitation kinetics that characterize systems with low initial dissolved SiO_2 concentration (Figure 31-A and Figure 32-A), whatever the investigated ionic strength and pH, is correctly caught, with a decrease of dissolved SiO_2 less than 1 mmol·kg^{-1} after ~ 4·10^5 s, that is about 4.5 days.

When the initial SiO_2 content is increased (Figure 31-B and Figure 32-B), weakly acid to neutral solutions (5 < pH < 7) are the most reactive. The dissolved SiO_2 decreases very rapidly to the stationary value of 2 mmol·kg^{-1}, with a quite short to very short lifetime for the nanocolloidal silica and a rapid precipitation of amorphous silica. From pH 5 to lower values, the lifetime of the nanocolloidal silica increases up to at least 14 days in low ionic strength solutions, which

hinders the formation of precipitated amorphous silica and slows down the decrease of dissolved silica with time. Higher ionic strengths tend to increase the lifetime of nanocolloidal silica and delay the formation of amorphous silica, in particular at pH 5-6 (dashed grey and yellow lines). At pH 3-4, and the 0.24 molal ionic strength, one must acknowledge that the model hardly reproduces the somehow rapid decrease of the dissolved SiO_2 concentration followed by a stabilization at a value of 6 mmol·kg^{-1}. Instead, the model describes a progressive decrease of dissolved SiO_2 down to concentrations around 6 mmol·kg^{-1} after $3 \cdot 10^5$ s, that is after about 3.5 days.

At even larger initial dissolved SiO_2 concentration (Figure 31-C and Figure 32-C), reactions kinetics are faster, which is correctly described by the proposed model.

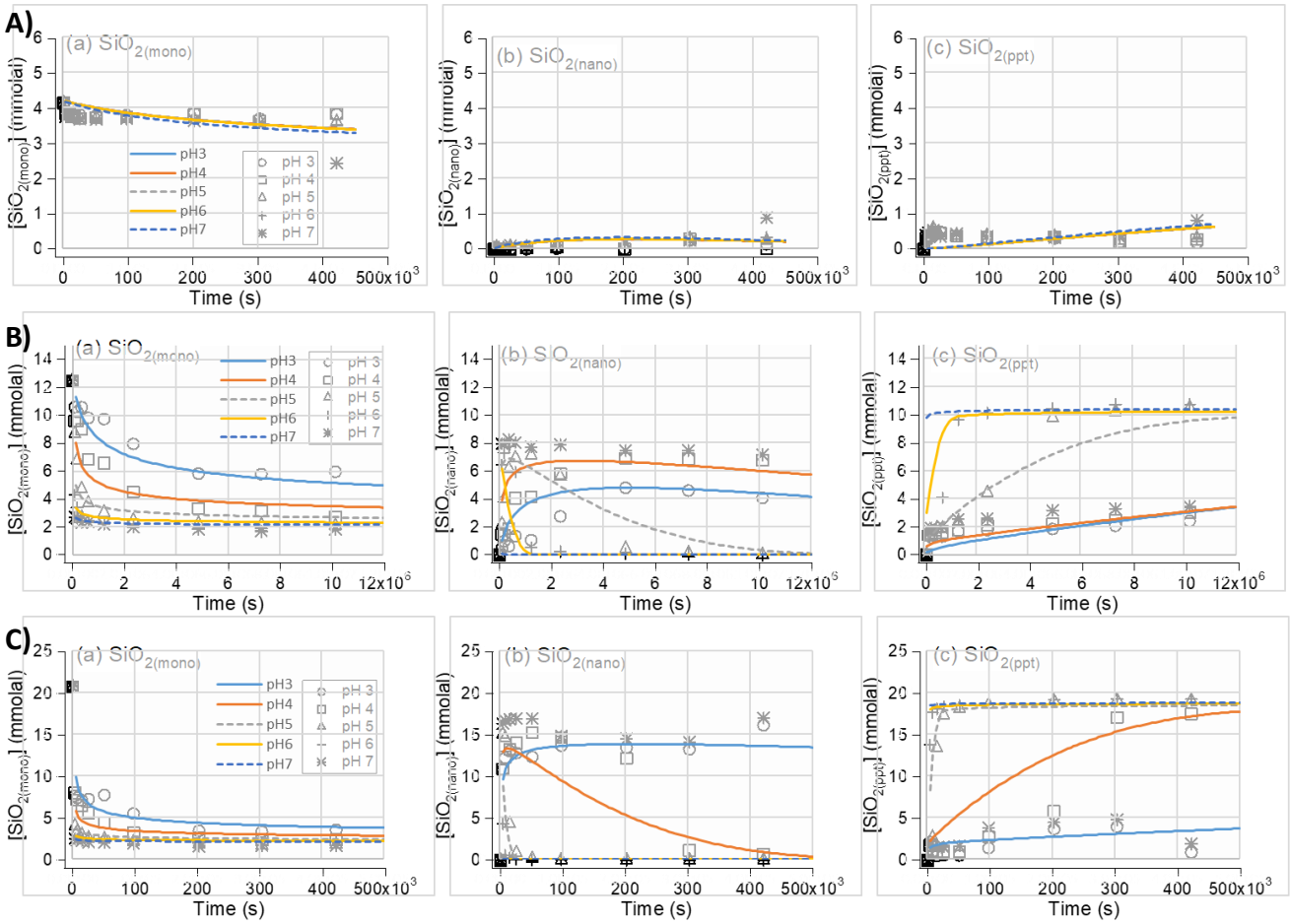

Figure 31: Evolution of dissolved monomeric silica (left), nanocolloidal silica (centre) and amorphous silica (right) concentrations vs. time, at pH 3, 4, 5, 6 and 7, in low ionic strength solutions (0.01 molal) and for various initial dissolved SiO_2 concentrations. A) 4.2 mmolal, B) 12.5 mmolal, C) 20.8 mmolal. Symbols: experimental data from Icopini et al. (2005); coloured lines: calculated with the proposed model. Modified after Conrad et al. (2007).

The next step in the evaluation of the model is to test it against experimental data acquired independently. Dixit et al. (2016) measured the precipitation kinetics of silica in aqueous solutions taken at the geothermal plant of Bouillante, Guadeloupe, France. The authors investigated various conditions of pH and temperature, from 5 to 8 and from 22 to 90°C, respectively. Besides, the chemical composition of the Bouillante waters correspond to a

dissolved silica content of 10 mmolal and an ionic strength of about 0.5 molal. Thus, part of the conditions investigated by Dixit et al. (2016) coincides with the domain of applicability of the model proposed in the present work, despite the ionic strength of the Bouillante waters is higher than in the experiments of Icopini et al. (2005).

The chemical composition of the solution used in the experiments of Dixit et al. (2016) is given in Table 6. The results of the direct application of our proposed kinetic laws at pH 5 to 8 are plotted in Figure 33. It should be noted first that the time duration of the experiments is less than 600 minutes, that is less than 36,000 seconds when the experiments of Icopini et al. (2005) lasted 450,000 seconds and more. Therefore, our model, which is built on the data from Icopini et al. (2005) is not expected to be much accurate at a smaller time scale. In addition, it should be kept in mind that the ionic strength of the Bouillante geothermal waters lays beyond the range of ionic strength considered to build our model.

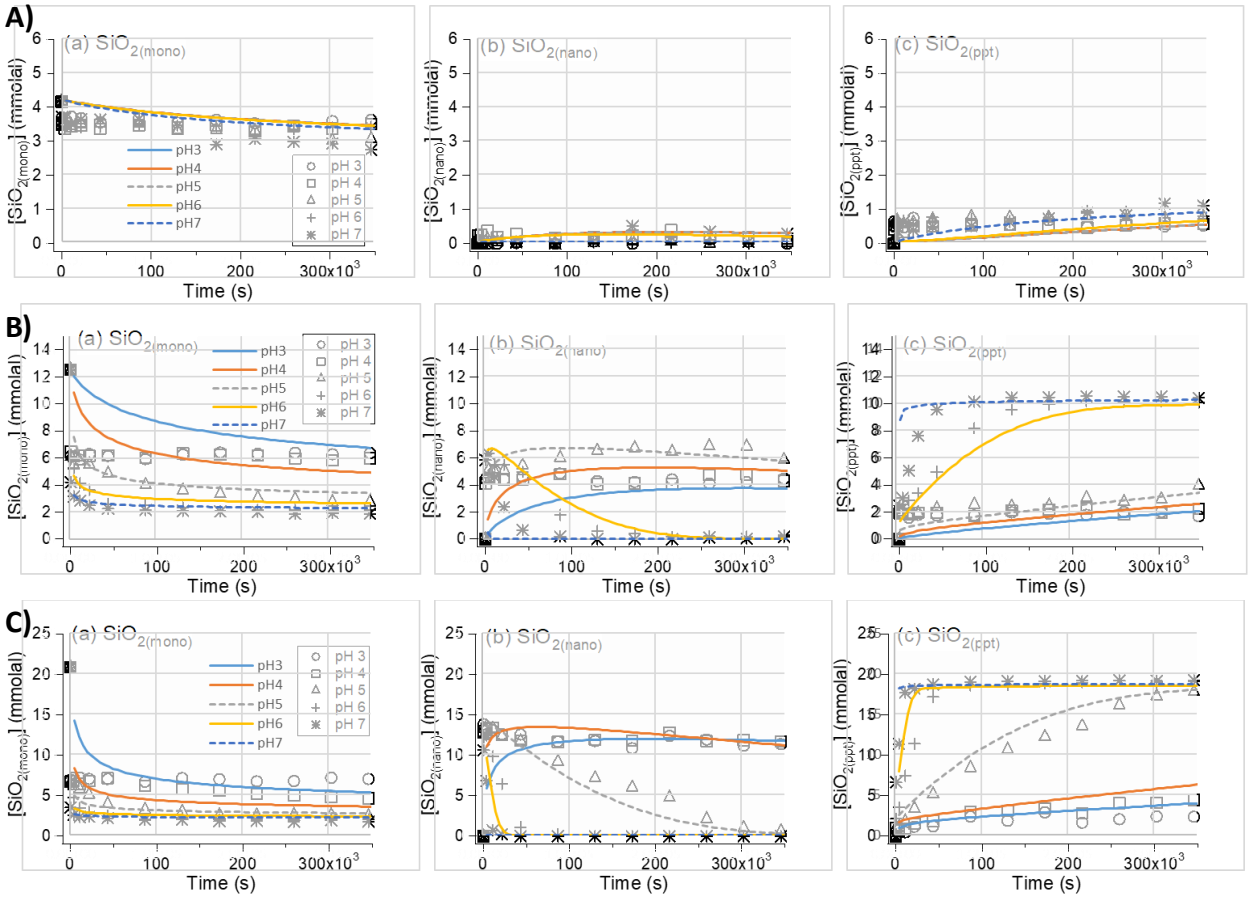

Figure 32: Evolution of dissolved monomeric silica (left), nanocolloidal silica (centre) and amorphous silica (right) concentrations vs. time, at pH 3, 4, 5, 6 and 7, in moderate ionic strength solutions (0.24 molal) and for various initial dissolved SiO_2 concentrations. A) 4.2 mmolal, B) 12.5 mmolal, C) 20.8 mmolal. Symbols: experimental data from Icopini et al. (2005); coloured lines: calculated with the proposed model. Modified after Conrad et al. (2007).

Therefore, Figure 33-A shows that our model overestimates the rate of decrease of dissolved silica concentration, especially at pH 5. However, the trend is respected since the concentration of dissolved silica stabilizes after about 600 minutes. The match with experimental data is better at pH 6 despite a faster consumption of dissolved silica simulated during the first hour. After about 300 minutes, simulated data are in good accordance with

experiments. Similarly, despite the kinetic law was developed for pH lower than 7, application up to pH 8 on the Bouillante waters shows that, except for the first hour, the experimental evolution of dissolved silica concentration with time can be reproduced very satisfactorily. Thus, it seems that the proposed model can be applied to such pH if the ionic strength of the solution is high enough, at least above 0.2 mol·kg^{-1}. These results are consistent with a decrease of the Debye length as ionic strength increases. A shorter Debye length allows nanoparticles to be in closer contact, with an increased probability to overcome the repulsive barrier, even though the negative charge at the surface of the particles increases compared to lower ionic strengths. Consequently, the repulsive pH effect is delayed to slightly higher pH values when ionic strength increases. Of course, at even larger pH values (above 7-8), it is expected that repulsion between particles further increases and thus prevents from aggregation.

Another observation concerns the chemical composition of the solutions studied. Indeed, those studied by Icopini et al. (2005) are synthetic, with element distribution compared to Bouillante waters. In Table 7, the chemical composition of the two types of water, normalized to the same Cl concentration, are tabulated for illustration. Elements are limited to the synthetic solutions, which include Na, K, Ca and C(+IV). Beyond ionic strength, the differences in chemical composition highlighted in Table 7 may affect the kinetics of silica precipitation.

Table 6: Chemical composition of the Bouillante geothermal water used in Dixit et al. (2016).

Element	Concentration (g·L^{-1})	Element	Concentration (mg·L^{-1})	Element	Concentration (mg·L^{-1})
pH	6.58 *	Br	51	Ba	7.7
Cl	14.651	CO_3	25.3	Mn	5.2
Na	6.331	SO_4	21.3	Li	4.9
Ca	2.217	Sr	18.1	Mg	1.9
K	0.944	B	14.6	F	1.3
Si	0.577			H_2S	0.68

*: unitless

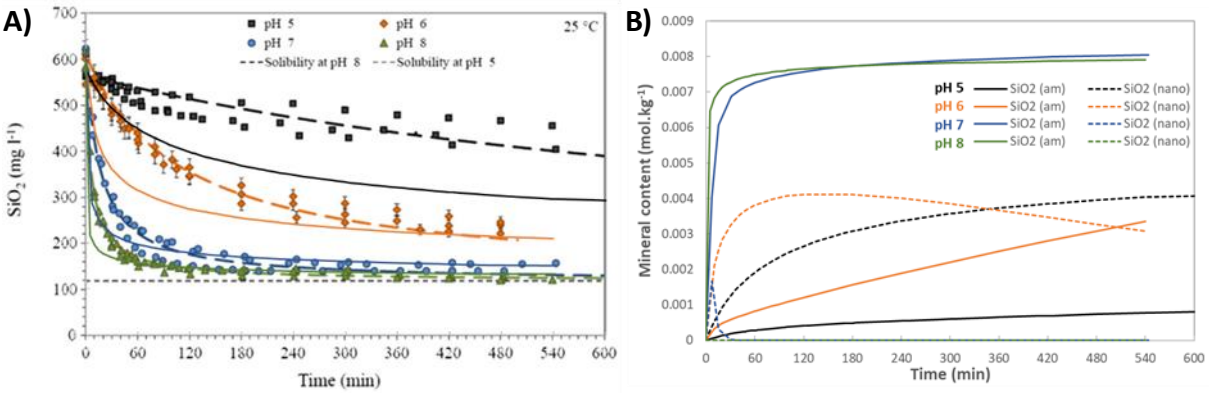

Figure 33: Evolution of dissolved monomeric silica (A), nanocolloidal silica and amorphous silica (B) concentrations vs. time, at pH 5 to 8, in Bouillante geothermal waters (0.47 molal ionic strength) at ~25°C. A) Symbols: experimental data from Dixit et al. (2016); coloured dashed lines: pH and temperature specific model of Dixit et al. (2016); full lines. Our model. B) Our model only.

Table 7: Comparison of the chemical compositions of the aqueous solutions used in the present work, normalized to the same Cl content (units in mmol·kg^{-1}).

Element	Na	K	Ca	Cl	C(+IV)
Icopini et al. (2005)	200	25.1	5	236	0.739
Dixit et al. (2016)	157	13.8	31.5	236	0.239

In addition, Figure 33-B provides information about the amounts of nanocolloidal silica and of amorphous silica. It suggests that, at the end of the experiment at pH 5, the precipitated silica should be mostly nanocolloidal and is still increasing. At pH 6, the decrease of the nanocolloidal silica starts in the 2nd hour and the amorphous silica starts becoming the majority at the end of the experiment. This latter result is in accordance with the observation of the mixture of particles of different size observed in Dixit et al. (2016). Unfortunately, the silica gel obtained at pH 5 has not been characterized by these authors and, thus, cannot be compared to our calculation results. At higher pH, simulations suggest that, if any, the lifetime of the nanocolloidal silica is very short.

4.4 SILICA DISSOLUTION

Part of the experiments performed in the framework of the REFLECT project are dealing with silica dissolution. Indeed, these experiments performed by IFE and described in paragraph 2.3 allow following the silica enrichment of the leaching solutions according to time. The previous model used for silica precipitation was not adapted for modelling such dissolution. However, many studies described the dissolution of silica according to temperature and saline conditions (Rimstidt and Barnes, 1980; Icenhower and Dove, 2000). Palandri and Kharaka (2004) also synthesized in a review the dissolution kinetics of many minerals including silica minerals like amorphous silica, quartz, cristobalite and chalcedony.

The first step consisted of use existing kinetic laws and to check if they match the experimental data. Initially, we started using kinetic laws devoted to quartz dissolution since sand grains of quartz fill in the columns of the experiments. However, some questions raised about the equilibrium silica concentration reached at the end of the experiments. Table 8 shows the equilibrium silica concentration of different silicate minerals calculated with Phreeqc code at 200°C and 50 and 300 g.L^{-1} (Parkhurst and Appelo, 2013). The calculations are done with the Thermoddem database (https://thermoddem.brgm.fr/ and Blanc et al., 2012). This database uses a B-dot approach as activity model. The equilibrium Si concentrations calculated with PhreeqC/Thermoddem are compared to silica concentration at the end of the experiments (conditions supposed to be close to the equilibrium). Consistently with the findings made in paragraph 2.3, the silica concentrations measured at equilibrium at the end of the experiments are similar to the equilibrium with amorphous silica. We do not have any explanation about this observation, except that the equilibrium silica concentrations with quartz are much lower than the measured data.

Table 8: Comparison between calculated and experimental silica concentrations at equilibrium state according to NaCl content and 200°C

NaCl concentration ($g.L^{-1}$)	Silica concentration at equilibrium ($mol.kg^{-1}$)			
	Amorphous silica*	Chalcedony*	Quartz*	Experiments
50	$1.28\ 10^{-2}$	$5.85\ 10^{-3}$	$3.89\ 10^{-3}$	$1.20\ 10^{-2}$
300	$8.83\ 10^{-3}$	$4.04\ 10^{-3}$	$2.68\ 10^{-3}$	$8.83\ 10^{-3}$

* calculated values with Phreeqc code

Consequently, the kinetic law that we used has to include the reference to amorphous silica:

$$rate_{diss} = S.m.M_{am.silica}.k_{neu}^{298.15}.e^{\frac{-E_{neut}}{R.(T-298.15)}}.(1-\Omega_{am.silica}) \qquad (9)$$

Where :

- S is the reactive surface area. The BET surface measured in this work (S = 0.69 $m^2.g^{-1}$) is used;
- $k_{neu}^{298.15}$ is the kinetic constant at 25°C and pH = 0. The value given by Rimstidt and Barnes (1980) is selected: $1.7\ 10^{-13}$ $mol.m^{-2}.s^{-1}$;
- m is the number of moles of amorphous silica (mol)
- $M_{am.silica}$ is the molecular mass of amorphous silica ($g.mol^{-1}$)
- E_{neut} is the activation energy. The value of Rimstidt and Barnes (1980) is selected: 68700 $kJ.mol^{-1}$
- T is temperature in Kelvin
- Ω is the mineral saturation index. It corresponds to the ratio Q/K, where Q is the product activity and K is the equilibrium constant.

By using this law, the model is able to reproduce the evolution of silica concentration in the solution according to amorphous silica dissolution (Figure 34). The model also takes into account the salinity of the solution: when the salinity increases the solubility decreases. It is the "salting-out" effect.

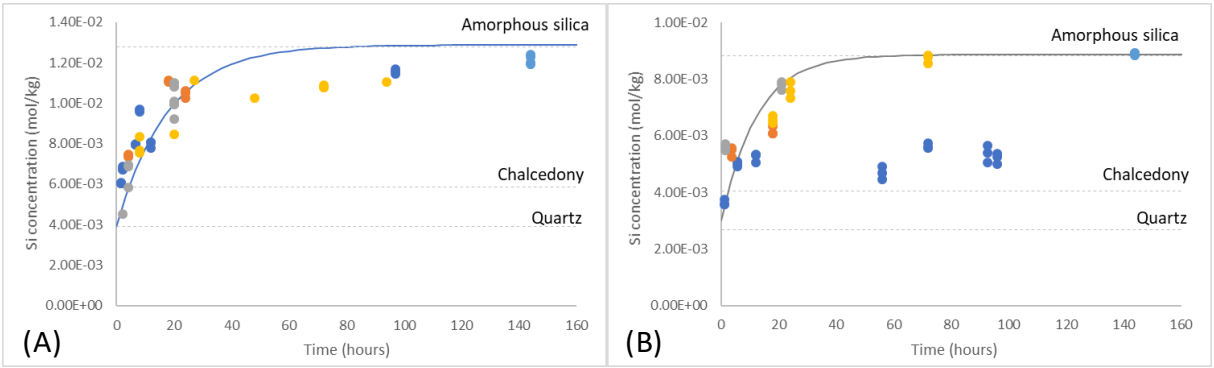

Figure 34: Evolution of dissolved silica (A) T = 200°C and [NaCl] = 50 $g.L^{-1}$; (B) T = 200°C and [NaCl] = 300 $g.L^{-1}$. Symbols: experimental data acquired in this study; Full lines: model; Dashed lines: calculated equilibrium silica concentration with amorphous silica, chalcedony and quartz

All the calculations are performed with a B-dot activity model. A Pitzer approach, dedicated to very high saline solutions, would probably be more appropriate to simulate the high NaCl content of the solution (300 $g.L^{-1}$). However, despite this approximation, the consistency with experimental data is acceptable.

4.5 CONCLUDING REMARKS

The proposed kinetic model for silica precipitation relies on simple relationships that link physical mechanisms (nucleation, aggregation, aging and growth) to physico-chemical parameters (pH, initial dissolved SiO_2, ionic strength). The range of conditions of application are the following: 3 < pH < 8, 0 < $m_{SiO_2}^{init}$ < 20.8 mmol·kg^{-1}, 0 < *I* < 0.5 mol·kg^{-1}, at 25°C.

Application to actual geothermal conditions is therefore not possible yet. Therefore, the work should be continued in order to include the effect of temperature, to cover larger ranges of ionic strength. In addition, recent experiments done by Dixit (pers. com.) show that the nature of the ions present in the solution does have an influence on the kinetic rate of silica precipitation, and more particularly on the induction time before the triggering of the precipitation process. These works, that were performed at 80°C could not be used in the present study, but they clearly indicate that specific terms should be implemented in the kinetic law to consider individually the role of the different cations. This would help improving the predictive capacity of the model for silica precipitation from a variety of geothermal brines.

5 CONCLUSIONS

The results achieved within this task in the REFLECT project have generally increased the knowledge of mineral solubility and precipitation at high salinity conditions in geothermal systems. The work has combined experimental work and numerical modelling to study silica solubility and precipitation as well as precipitation of calcite.

In subtask 2.3.1 an experimental setup for investigating mineral solubility at high salinity conditions was designed and tested. The setup was further used to perform experiments to study silica solubility and kinetics in the temperature range 100 to 200°C and NaCl concentration range 50.92 to 338.09 g/kg H_2O. Two types of experiments were performed, one to study silica solubility at equilibrium conditions and one to study solubility kinetics. The aim of the study is to increase the knowledge of solubility and precipitation of silica at high saline conditions. The main findings from the equilibrium solubility study are that silica solubility increases with temperature and decreases with salinity. Results from the kinetic experiments corresponds well with the results from the study performed at equilibrium conditions. However, as for the equilibrium results, the results obtained matches with values for amorphous silica obtained using modelling tool developed in subtask 2.3.3, not quartz as expected from initial XRD measurements.

In subtask 2.3.2 a conductivity probe was designed and tested for conductometric monitoring of calcite solubility and precipitation experiments in batch reactors in a temperature range of 24 - 215 °C at a maximum system pressure of 70 bar. Experiments addressed both the general lack of data on calcite solubility in high-temperature, high-salinity brines as well as related kinetic information. The main findings from the equilibrium solubility study are that calcite solubility decreases with temperature and increases with CO_2 pressure. Regarding salinity, the solubility of calcite in NaCl bearing fluids increases to a maximum between 5 - 10 wt% NaCl

and decreases again at higher salinity. Where available, values obtained, correspond well with literature data. The rate of calcite precipitation is found to depend on the decompression rate, and availability of seed crystals as well as their size. Due to a lack of time, the influence of other factors, such as flow rates (stirring rate), on the calcite precipitation rate was not examined in this study.

In subtask 2.3.3 a modelling approach was applied to follow both precipitation and dissolution kinetics of silica.
First, a model for silica precipitation was developed that accounts for several mechanisms, including nucleation, aggregation, aging and growth. The model describes the formation of both nanocolloidal and microscopic amorphous silica, and the evolution of their relative amounts with time. Mechanisms involved in the silica precipitation depend on main parameters like pH, initial dissolved silica content ($m_{SiO_2}^{init}$) and ionic strength (I). If the model was calibrated on literature data that were obtained from experiments made on synthetic solutions, it was tested during this study on literature data issued from real geothermal waters. The results highlight that the model is actually valid in the following range of conditions of application: $3 < pH < 8$, $0 < m_{SiO_2}^{init} < 20.8$ mmol·kg^{-1}, $0 < I < 0.5$ mol·kg^{-1}, at 25 °C. Next developments should allow extending the model to higher temperature conditions.
The modelling work also allowed simulating the quartz dissolution experiments done by partners in subtask 2.3.1. Modelling used a kinetic rate law based on the transition state theory. By using this law, the model is able to reproduce the evolution of silica concentration in the solution with time and the final equilibrium state according to amorphous silica dissolution. These results suggest that, despite the sand used for the experiments was made of quartz, the measured SiO_2 concentrations rather correspond to amorphous silica. The present experimental and numerical investigations cannot explain why the amorphous silica is controlling the kinetics.

6 REFERENCES

References Section 2:

Cournoyer, R.A, Kranich, W.L and Sand, L.B, 1975. Zeolite crystallization kinetics related to dissolution rates of quartz reactant, *J. Phys. Chem*, 79, 1578-1581.

Dixit, C., Bernard, M.L., Sanjuan, B., André, L. and Gaspard, S., 2016. Experimental study on the kinetics of silica polymerization during cooling of the Bouillante geothermal fluid (Guadeloupe, French West Indies), *Chemical Geology*, 442, 97-112.

Dove, P.M and Rimstidt, J.D, 1994. *Chapter 8: Silica-water interactions, in Silica: physical behaviour, geochemistry and materials applications*, Edited by Heaney, P.J, Prewitt, C.T. and Gibbs, G.V.

Driesner, T and Heinrich, C.A., 2007. The system H2O–NaCl. Part I: Correlation formulae for phase relations in temperature–pressure–composition space from 0 to 1000°C, 0 to 5000bar, and 0 to 1 XNaCl, *Geochimica et Cosmochimica Acta*, 71, 4880-4901.

Heitmann, H.G, 1964, Solubility of silicic acid in water and steam and their influence on turbine silication, *Chemiker Ztg./Chem. Apperatur*, 88, 891-893.

Rimstidt, J.D. and Barnes, H.L., 1980. The kinetics of silica-water reactions, *Geochimica et Cosmochimica Acta*, 44, 1683-1699.

Tester, J.W., Worley, W.G., Robinson, B.A., Grigsby, C.O. and Feerer, J.L., 1994. Correlating quartz dissolution kinetics in pure water from 25 to 625°C, *Geochimica et Cosmochimica Acta*, 58, 2407-2420.

Van Lier, J.A, de Bruyn, P.L and Overbeek, J.T.G, 1960. The solubility of quartz, *J. Phys. Chem*, 35, 423-434.

Von Damm, K.L, Bischoff, J.L and Rosenbauer, R.J, 1991, Quartz solubility in hydrothermal seawater: an experimental study and equation describing quartz solubility for up to 0.5 M NaCl solutions, *American Journal of Science*, 291, 977-1007

References Section 3:

Arnórsson, S., 1981. Mineral deposition from Icelandic geothermal waters, environmental and utilization problems, J. Petroleum Technology, 33 (1), 181-187.

Arnórsson, S., 1989. Deposition of calcium carbonate minerals from geothermal waters — theoretical considerations, Geothermics, 18, 33-39.

Atkinson, G., Oklahoma, U., Raju, K., Aramco, S., and Howell, R.D., 1985. The thermodynamics of scale prediction, SPE International Symposium on Oilfield Chemistry, Anaheim, California, February 1991, SPE-21021-MS, (1991), 209-215 Baumann, J. Buhmann, D., Dreybrodt, W. and Schulz. H.D.: Calcite dissolution kinetics in porous media, *Chem. Geol.*, 53, 219-228.

Bychkov, A.Yu., Bénézeth, P., Pokrovsky, O.S., Shvarov, Yu.V., Castillo, A. and Schott, J., 2020. Experimental determination of calcite solubility and the stability of aqueous Ca- and Na-carbonate and -bicarbonate complexes at 100-160 °C and 1-50 bar pCO_2 using in situ pH measurements, *Geochim. Cosmochim. Acta*, 290, 352-365.

Coto, B., Martos, C., Peña, J.L., R. Rodríguez, R. and Pastor, G., 2012. Effects in the solubility of $CaCO_3$: Experimental study and model description, *Fluid Phase Equilibria*, 324, 1-7.

Dreybrodt, W., Lauckner, J., Liu, Z., Svensson, U. and Buhmann, D., 1996. The kinetics of the reaction $CO_2 + H_2O$ —> $H+ + HCO_3-$ as one of the rate limiting steps for the dissolution of calcite in the system H_2O-CO_2-$CaCO_3$, Geochim. Cosmochim. Acta, 60, 3375-3381.

Eisenlohr, L., Meteva, K., Gabrovšek, F., Dreybrodt, W., 1999. The inhibiting action of intrinsic impurities in natural calcium carbonate minerals to their dissolution kinetics in aqueous H_2O–CO_2 solutions. *Geochimica et cosmochimica acta*, *63*(7-8), 989-1001.

Ellis, A.J., 1959. The solubility of calcite in carbon dioxide solutions, *Amer. J. Sci.*, 257, 354-365.

Ellis, A.J., 1963. The solubility of calcite in sodium chloride solutions at high temperature, *Amer. J. Sci.*, 261, 259-267.

Haklidir, F.S.T. and Balaban, T.Ö., 2019. A review of mineral precipitation and effective scale inhibition methods at geothermal power plants in West Anatolia (Turkey), Geothermics, 80, 103-118.

Hastings, A.B., Murray; C.D. and Sendroy Jr., J., 1927. Studies of the solubility of calcium salts. I. The solubility of calcium carbonate in salt solutions and biological fluids, *J. Biolog. Chem.*, 71 (3), 723-781.

Kendall, J., 1912. The solubility of calcium carbonate in water, *T. Philos. Mag. Ser.*, 23 (6), 958-976.

Kindyakov, P.S., Khokhlova, A.V. and Lapchinskaya, L.L., 1958. Solubility in the reciprocal system lithium carbonate-calcium hydrate-water., *Tr. Mosk. Inst. Tonkoi Khim. Tekhnol.*, 7, (1958), 32-44.

Köhl, B., Grundy, J., Baumann, T., 2020. Rippled Scales in a Geothermal Facility in the Bavarian Molasse Basin: A Key to Understand the Calcite Scaling Process. Geotherm. Energy, 8, 1–27.

Li, Y., 2017. Calcite scaling potential of Kangding geothermal field, W-Sichuan plateau, China, United Nation University - Geothermal training program 2017, IS-108 Reykjavik, Iceland, Reports 2017 # 16.

MacDonald, R.W. and North, N.A., 1974. The Effect of Pressure on the Solubility of $CaCO_3$, CaF_2, and $SrS0_4$ in Water, *Can. J. Chemistry*, 52 (18), 3181-3186.

Malinin, S.D. and Kanukov, A.B., 1971. The solubility of calcite in homogeneous H_20-NaCl-CO_2 systems in the 200-600 °C temperature interval, *Geochem. Internat.*, 8, 668-679.

Miller, J.P., 1952. A portion of the system calcium carbonate–carbon dioxide–water, with geological implications, *Am. J. Sci.*, 250, 161-203.

Plummer, L.N., and Busenberg, E., 1982. The solubilities of calcite, aragonite and vaterite in CO_2-H_2O solutions between 0 and 90 °C, and evaluation of the aqueous model for the system $CaCO_3$-CO_2 -H_2O, *Geochim. Cosmochim. Acta*, 46, 1301-1331.

Quinao, J.J., Buscarlet, E., and Siega, F., 2017. Early identification and management of calcite deposition in the Ngatamariki geothermal field, New Zealand, Proceedings of 42nd Workshop on Geothermal Reservoir Engineering 2017, Stanford University, Stanford, USA, paper SGP-TR-212, 9 p.

Segnit, E.R., Holland, H.D., and Biscardi, C.J., 1962. The solubility of calcite in aqueous solutions. I. The solubility of calcite in water between 75 degrees and 200 degrees at CO_2 pressures up to 60 atm, *Geochim. Cosmochim. Acta*, 26, 1011-1040.

Svensson, U. and Dreybrodt, W., 1992. Dissolution kinetics of natural calcite minerals in CO2-water systems approaching calcite equilibrium. *Chemical Geology*, *100*(1-2), 129-145.

Vosbeck, K., 2004. Experimentelle Bestimmung der Lösungskinetik synthetischer Calciumcarbonate und natürlicher Kalkgesteine, Dissertation, *University of Bremen*, Germany, 111 p.

Wanner, C., Eichinger, F., Jahrfeld, T., and Diamond, L.W., 2017. Causes of abundant calcite scaling in geothermal wells in the Bavarian Molasse Basin, Southern Germany, Geothermics, 70, 324-338.

Weyl, P.K., 1959. The change in solubility of calcium carbonate with temperature and carbon dioxide content, *Geochim. Cosmochim. Acta*, 17, 214-225.

Weyl, P.K., 1966. The solution behavior of carbonate materials in sea water, *EPR Publ.*, 428, Shell Development Co., Houston, 59 p.

Wigley, T. M. L. and Plummer, L. N., 1976. Mixing of carbonate waters. Geochimica et Cosmochimica Acta, 40(9), 989-995.

Wolf, M., Breitkopf, O. and Puk R., 1989. Solubility of calcite in different electrolytes at temperatures between 10 and 60°C and at CO_2 partial pressures of about 1 kPa, *Chem. Geol.*, 76, 291–301.

Yanatéva, O.K., 1955. Solubility in the system $CaCO_3$-$MgCO_3$-H_2O at different temperatures, *Zhurnal Neorganicheskoi Khimii*, 1, 1473-1476.

References Section 4:

André, L., Devau, N., Pedenaud, P., Azaroual, M., 2017. Silica Precipitation Kinetics: The Role of Solid Surface Complexation Mechanism Integrating the Magnesium Effects from 25 to 300°C. Procedia Earth Planet. Sci. 17, 217–220. https://doi.org/10.1016/J.PROEPS.2016.12.075

Blanc, P., Lassin, A., Piantone, P., Azaroual, M., Jacquemet, N., Fabbri, A., and Gaucher, E. C., 2012, Thermoddem: A geochemical database focused on low temperature water/rock interactions and waste materials: Appl. Geochem. 27, 2107-2116. https://doi.org/10.1016/j.apgeochem.2012.06.002

Conrad, C.F., Icopini, G.A., Yasuhara, H., Bandstra, J.Z., Brantley, S.L., Heaney, P.J., 2007. Modeling the kinetics of silica nanocolloid formation and precipitation in geologically relevant aqueous solutions. Geochim. Cosmochim. Acta 71, 531–542. https://doi.org/10.1016/j.gca.2006.10.001

Dideriksen, K., Frandsen, C., Bovet, N., Wallace, A.F., Sel, O., Arbour, T., Navrotsky, A., De Yoreo, J.J., Banfield, J.F., 2015. Formation and transformation of a short range ordered iron carbonate precursor. Geochim. Cosmochim. Acta 164, 94–109. https://doi.org/10.1016/j.gca.2015.05.005

Dixit, C., Bernard, M.-L., Sanjuan, B., André, L., Gaspard, S., 2016. Experimental study on the kinetics of silica polymerization during cooling of the Bouillante geothermal fluid (Guadeloupe, French West Indies). Chem. Geol. 442, 97–112. https://doi.org/10.1016/J.CHEMGEO.2016.08.031

Dove, P., Icenhower, J., 1997. Kinetic and thermodynamic controls on silica reactivity: an analog for waste disposal media. Presented at the CEA/Valrho summer session. Glass scientific research for high performance containment, Mejannes-Le-Clap (France).

Eyring, H., 1935. The Activated Complex in Chemical Reactions. J. Chem. Phys. 3, 107–115. https://doi.org/10.1063/1.1749604

Forbes, T.Z., Radha, A.V., Navrotsky, A., 2011. The energetics of nanophase calcite. Geochim. Cosmochim. Acta 75, 7893–7905. https://doi.org/10.1016/j.gca.2011.09.034

Icopini, G.A., Brantley, S.L., Heaney, P.J., 2005. Kinetics of silica oligomerization and nanocolloid formation as a function of pH and ionic strength at 25°C. Geochim. Cosmochim. Acta 69, 293–303. https://doi.org/10.1016/j.gca.2004.06.038

Jiang, S., Pan, H., Chen, Y., Xu, X., Tang, R., 2015. Amorphous calcium phosphate phase-mediated crystal nucleation kinetics and pathway. Faraday Discuss. 179, 451–461.

Lasaga, A.C., 1981. Transition state theory. Rev. Mineral. Geochem. 8, 135–168.

Lassin, A., André, L., Devau, N., Lach, A., Beuvier, T., Gibaud, A., Gaboreau, S., Azaroual, M., 2018. Dynamics of calcium carbonate formation: geochemical modeling of a two-step mechanism. Geochim. Cosmochim. Acta 240, 236–254. https://doi.org/10.1016/J.GCA.2018.08.033

Parkhurst, D.L., and Appelo, C.A.J., 2013, Description of input and examples for PHREEQC version 3—A computer program for speciation, batch-reaction, one-dimensional transport, and inverse geochemical calculations: U.S. Geological Survey Techniques and Methods, book 6, chap. A43, 497 p., available only at http://pubs.usgs.gov/tm/06/a43/.

Radha, A.V., Fernandez-Martinez, A., Hu, Y., Jun, Y.-S., Waychunas, G.A., Navrotsky, A., 2012. Energetic and structural studies of amorphous Ca1− xMgxCO3· nH2O (0⩽ x⩽ 1). Geochim. Cosmochim. Acta 90, 83–95.

Radha, A.V., Forbes, T.Z., Killian, C.E., Gilbert, P.U.P.A., Navrotsky, A., 2010. Transformation and crystallization energetics of synthetic and biogenic amorphous calcium carbonate. Proc. Natl. Acad. Sci. U. S. A. 107, 16438–16443.

Rimstidt, J.D., Barnes, H.L., 1980. The kinetics of silica-water reactions. Geochim. Cosmochim. Acta 44, 1683–1699. https://doi.org/10.1016/0016-7037(80)90220-3

Ruiz-Agudo, C., Avaro, J.T., Schupp, D.J., McDonogh, D., Gebauer, D., 2020. Capturing an amorphous BaSO4 intermediate precursor to barite. CrystEngComm 22, 1310–1313. https://doi.org/10.1039/c9ce01555h

Sel, O., Radha, A.V., Dideriksen, K., Navrotsky, A., 2012. Amorphous iron (II) carbonate: Crystallization energetics and comparison to other carbonate minerals related to CO2sequestration. Geochim. Cosmochim. Acta 87, 61–68. https://doi.org/10.1016/j.gca.2012.03.011

Setiawan, F.A., Rahayuningsih, E., Petrus, H.T.B.M., Nurpratama, M.I., Perdana, I., 2019. Kinetics of silica precipitation in geothermal brine with seeds addition: minimizing silica scaling in a cold re-injection system. Geotherm. Energy 7, 22–22. https://doi.org/10.1186/s40517-019-0138-3

Van Driessche, A.E.S., Benning, L.G., Rodriguez-Blanco, J.D., Ossorio, M., Bots, P., García-Ruiz, J.M., 2012. The role and implications of bassanite as a stable precursor phase to gypsum precipitation. Science 335, 69–72. https://doi.org/10.1126/science.1215648